The Influence of Dome Size, Parent Vessel Angle, and Coil Packing Density On Coil Embolization Treatment in Cerebral Aneurysms

by

Aprinda Indahlastari

A Thesis Presented in Partial Fulfillment
of the Requirements for the Degree
Master of Science

Approved July 2013 by the
Graduate Supervisory Committee:

David Frakes, Chair
Brian Chong
Jitendran Muthuswamy

ARIZONA STATE UNIVERSITY

August 2013

ABSTRACT

A cerebral aneurysm is a bulging of a blood vessel in the brain. Aneurysmal rupture affects 25,000 people each year and is associated with a 45% mortality rate. Therefore, it is critically important to treat cerebral aneurysms effectively before they rupture. Endovascular coiling is the most effective treatment for cerebral aneurysms. During coiling process, series of metallic coils are deployed into the aneurysmal sack with the intent of reaching a sufficient packing density (PD). Coils packing can facilitate thrombus formation and help seal off the aneurysm from circulation over time. While coiling is effective, high rates of treatment failure have been associated with basilar tip aneurysms (BTAs). Treatment failure may be related to geometrical features of the aneurysm. The purpose of this study was to investigate the influence of dome size, parent vessel (PV) angle, and PD on post-treatment aneurysmal hemodynamics using both computational fluid dynamics (CFD) and particle image velocimetry (PIV).

Flows in four idealized BTA models with a combination of dome sizes and two different PV angles were simulated using CFD and then validated against PIV data. Percent reductions in post-treatment aneurysmal velocity and cross-neck (CN) flow as well as percent coverage of low wall shear stress (WSS) area were analyzed. In all models, aneurysmal velocity and CN flow decreased after coiling, while low WSS area increased. However, with increasing PD, further reductions were observed in aneurysmal velocity and CN flow, but minimal changes were observed in low WSS area. Overall, coil PD had the greatest impact while dome size has greater impact than PV angle on aneurysmal hemodynamics. These findings lead to a conclusion that combinations of treatment goals and geometric factor may play key roles in coil embolization treatment outcomes, and support that different treatment timing may be a critical factor in treatment optimization.

TABLE OF CONTENTS

Page

LIST OF TABLES

Table Page

LIST OF FIGURES

Figure Page

Chapter 1: INTRODUCTION

Background

An aneurysm is a vascular disorder characterized by a localized dilation in a blood vessel. As the aneurysm starts to grow, the endothelial cell lining along the arterial or venous wall, where the aneurysm is formed, continues to weaken (Ross et al., 2007). A cerebral aneurysm is a specific case of an aneurysm where the blood vessel dilation is formed in the brain. Aneurysmal growth can eventually lead to aneurysmal rupture causing blood to flow out of the cerebrovascular system and into the surrounding brain tissues, also known as a subarachnoid hemorrhage (SAH). This condition can cause a serious hemorrhagic stroke and lead to severe brain damage or death. Approximately 25,000 people in the US suffer from SAH each year, and 2% of the population is at risk of having SAH (Ross et al, 2007). Ruptured cerebral aneurysms are associated with a 45% mortality rate; therefore, it is ideal to treat aneurysms effectively before they rupture (Bederson et al., 2009).

Intracranial aneurysms (ICAs) most often occur in major arteries in the Circle of Willis in variety of shapes. The Circle of Willis is a loop at the base of the brain consisting of the internal carotid artery, the anterior cerebral arteries (branches of the internal carotid artery), the middle cerebral arteries, the posterior cerebral arteries (branches of the basilar artery), and the basilar artery (Figure 1). Two common shapes of ICAs are fusiform and saccular. Fusiform ICAs are axisymmetric, non-saccular dilation surrounding the entire vessel wall over a short distance usually occurs in the internal carotid artery. Saccular ICAs are spherical in shape and usually occur at major bifurcations or branch points of arteries at the base of the brain, such as at the tip of the basilar artery bifurcation (Barret, 2006).

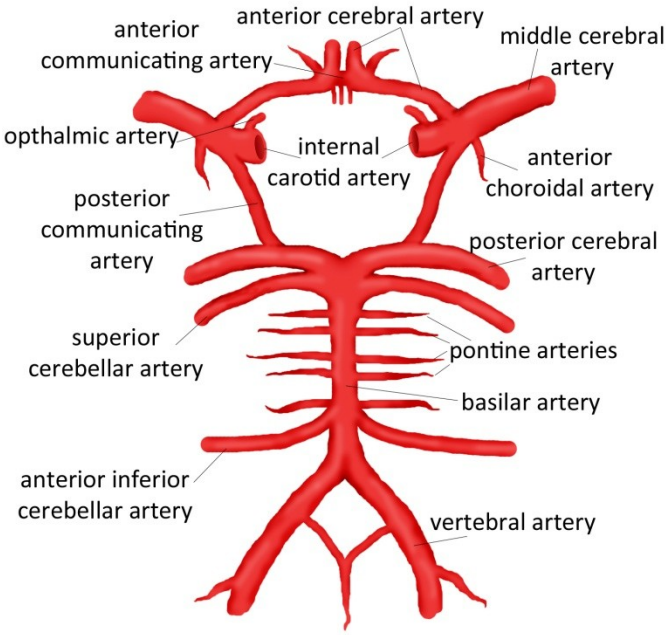

Figure 1. The anatomy of the Circle of Willis[1].

Even though treatment options and prevention actions surrounding ICAs have been studied rigorously, the factors that cause an aneurysm to form are still unclear. A combination of endogenous and exogenous factors was found to cause aneurysm occurrence. The endogenous factors such as elevated arterial blood pressure, the geometric anatomy of the Circle of Willis, and hemodynamic patterns originating at vessel bifurcation along with exogenous factors such as alcohol consumption, cigarette smoking and prescribed medications have been found to contribute to the occurrence of brain aneurysms. ICAs could also form as a result of an inborn genetic defect, which has been debated at length for over a decade (Ding et al., 2008). However, treating aneurysms before rupture is essential regardless of how they are formed.

[1] "Chapter 3." Children's Hospital of Wisconsin in Milwaukee, WI, is a member of Children's Hospital and Health System - Home Page. http://www.chw.org/display/PPF/DocID/48513/router.asp

Basilar Tip Aneurysm

Basilar tip aneurysms (BTAs) refer to saccular aneurysm formations at the tip of the basilar artery bifurcation and are associated with high treatment failure rates. The brain relies on two major arteries for blood supply: the carotid and vertebral arteries. The vertebral arteries are joined to form a single basilar artery at the base of the Circle of Willis, which eventually bifurcates into left and right posterior cerebral arteries. At the tip of this bifurcation anatomy is where the BTAs are formed. Even though BTAs have a 4-5% chance of occurrence, they are the most difficult to treat surgically when comparing to other ICA locations in the Circle of Willis. BTA treatment is associated with a 47.4% mortality rate (Krisht et al., 2007). High treatment failure rates associated with BTAs may be correlated with the complex bifurcation geometry. A high velocity jet stream coming from the vertebral arteries also contributes to BTAs formation and rupture. (Ford et al., 2008)

Endovascular Treatments

The main goal in treating ICAs prior to and post-rupture is to prevent blood flow from entering the aneurysmal sac by excluding the sac from blood circulation. Neurosurgical clipping and endovascular treatment are the two main treatment options for cerebral aneurysms as shown in Figure 2. Neurosurgical clipping is a procedure to place a small, metal like clip across the aneurysmal neck to prevent blood from traveling into the aneurysmal sac (Frosting et al., 2001). This procedure is an invasive one as the neurosurgeon removes part of the skull to locate and clip the aneurysm. Even though skull removal has been replaced by an eyebrow incision to access the aneurysm location, the clipping procedure is still considered invasive and is highly prone to surgical complications (Lusseveld et al., 2002). Alternatively, endovascular treatments offer a

less invasive treatment option (Geyik et al., 2007). Endovascular treatments involve deploying a device at the aneurysm site by navigating a microcatheter containing the device via a femoral artery. These devices can lead to flow stagnation within the aneurysm, promoting thrombosis. Endovascular coiling is the most common treatment for cerebral aneurysms and is generally most effective among available options (Geyik et al. 2007).

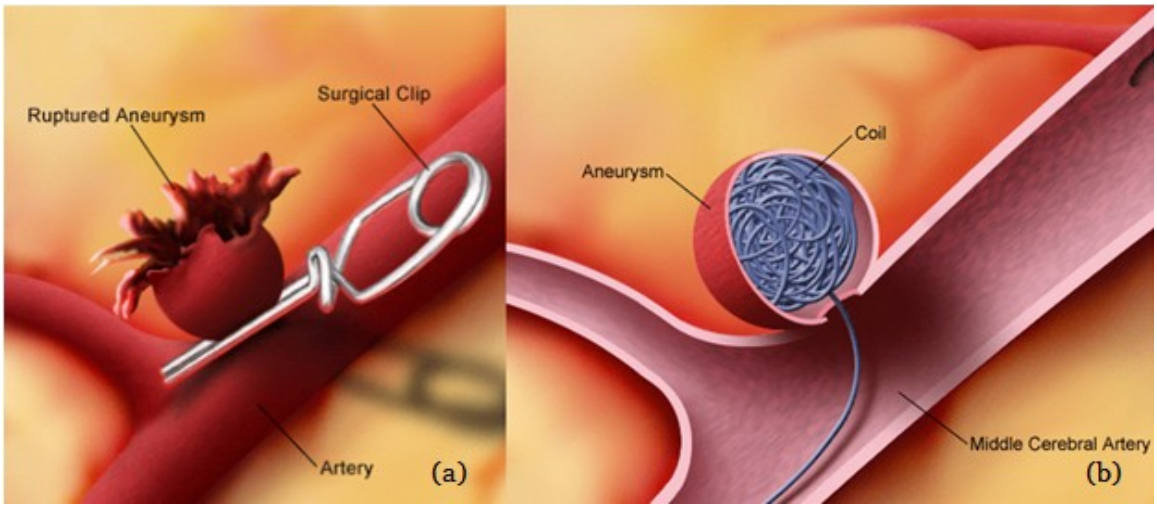

Figure 2. The two treatment options for ICAs namely surgical clipping (a) and embolic coils (b)[2].

During coil embolization, series of metallic coils of different sizes and shapes are deployed in a patient during surgery under a fluoroscopy machine. The neurosurgeon utilizes x-ray visualization and high-speed radiographic filming techniques to navigate the catheter. The coil deployment begins with the insertion of a guide wire into a selected artery to place a catheter. After the catheter is placed, the guide wire is retracted and a contrast dye is injected into the catheter to locate the aneurysm through an angiogram. Once the aneurysm location is found, a microcatheter containing coils is placed inside

[2] "Endovascular Coiling." Yale Medical Group. http://www.yalemedicalgroup.org/stw/Page.asp?PageID=STW029076.

the initial catheter and coils are deployed at the center of the aneurysmal dome. Once aneurysm is packed with the desired numbers of coils, the catheter system is removed and the procedure is complete. A balloon or a stent may be used for wide neck aneurysms to prevent coils from herniating into the parent vessel.

Coil packing density (PD) is a quantitative measure of coil packing that is considered to correlate with treatment success (Ding et al. 2008). Platinum coils are made out of a very thin metal wire and is wound longitudinally so it has an outer diameter D1 and a length L. Each coil is also designed to have a variation of loop coil diameter D2, as shown in Figure 3, so that it can fill up the aneurysmal dome more efficiently. Packing density is calculated by dividing the coil volume by the aneurysmal volume (1.1), where the coil volume is a cylindrical volume consists of D1 and L (1.2).

$$\% PD = \frac{Volume_{coil}}{Volume_{aneurysm}} x\ 100 \quad (1.1)$$

$$\text{and} \quad Volume_{coil} = \frac{1}{4}\ \pi\ D_1\ L \quad (1.2)$$

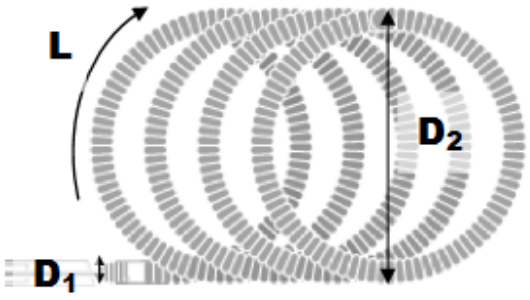

Figure 3. Coil dimension where L, D1, and D2 refer to coil length, outer diameter and loop diameter, respectively.

Coil deployments usually start from a larger D2 to form a basket that frames the outer most circumference inside the aneurysmal dome, and then continue to a smaller D2 to fill the empty space in between the larger coils. There are two basic types of coils based on their pre-programmed shape: helical and complex. Complex coils are believed to improve the recanalization rate and can achieve higher PD compared to helical coils (Wakhloo et al. 2007). There is no exact protocol on which PD to use on a patient since it varies on patient's case by case basis. In fact, higher PD does not necessarily give better treatment outcomes. (Ding et al., 2008)

Computational Simulation

Computational simulation has been used widely to determine hemodynamic properties by using a numerical approach, and it provides quantifications that are difficult to achieve during experimentation. Experimental fluid visualization and analysis technique delivers very detailed measurements; however, it still has a number of limitations. Particle image velocimetry (PIV), for instance, provides a good visualization of flow dynamics inside an aneurysm model for most cases, but it is not satisfactory when it comes to investigating flow inside aneurysm that has been treated with certain types of endovascular device such as embolic coils. It is difficult to measure hemodynamic changes inside the aneurysm due to laser occlusion and reflections caused by the metallic material of the coils. The laser light is greatly reflected once the model is illuminated by a laser sheet. Moreover, the particles tend to stick to the metallic coils, causing them to clump. The aggregated particles will be removed during PIV processing, since they are stationary. Therefore, capturing fluid dynamic information inside aneurysmal dome with embolic coils using the PIV technique is limited.

Computational simulation process can be automated by using scripts allowing different hemodynamic scenarios to be completed in a shorter time compared to experimental work. CFD is an example of such computational tool that has been widely used to simulate hemodynamics in aneurysms. While it has been commonly used, modeling post-treatment hemodynamics still remains a challenge, particularly in modeling device geometry and deployment. Finite element (FE) modeling can be used to simulate virtual deployments and provide post-deployment geometry based on the structural properties and design specification. Therefore, a combination of CFD and FE modeling can be used to study post-treatment hemodynamics in different aneurysmal geometric features and cases.

Finite Element Analysis

Finite element (FE) analysis is a tool to approximate an infinite dimensional system by defining degrees of freedom. FE modeling is a numerical approximation technique to divide a solid structure into discrete regions based on its geometry, material properties, loading and boundary conditions. These discrete regions, known as elements, are defined by nodes. These nodes carry a different density based on the anticipated stress levels of different elements, and their physical values can be found by interpolations. There are different types of elements that can be simulated through FE analysis software such as beam, rod, and shell elements.

FE analysis begins by dividing a structure into elements with nodes (discretization) then connects individual elements to form a system of equations in matrices. Each element within this system of equation contains different material properties and displacements that can be calculated. FE method calculates solutions to the system of equations based on the principle of virtual work, which states that any

particles under a set of a system of forces has a virtual work of zero for any given displacement in a equilibrium phase. Each variable, e.g., internal forces exerted by the nodes within each element, can be solved, and the global forces of the internal and external forces are calculated as the overall solution to the entire structure.

The governing equation of FE modeling is the equation of motion (1.3a). This equation consists of a mass matrix *[M]* multiplied by acceleration $\ddot{u}$, dampening matrix *[D]* multiplied by velocity $\dot{u}$, and stiffness matrix *[K]* multiplied by displacement u. There are two methods to solve the equation of motion: implicit and explicit methods. Implicit method is an iterative method where the displacement is not a function of time so that the velocity and acceleration terms, which are time derivatives, are discarded. Therefore, the implicit method solution depends solely on the stiffness matrix. This method can be inefficient in terms of computational time if the stiffness matrix size is large. Explicit method, on the other hand, is time dependent (dynamic approach) and non-iterative. This method is utilized to solve large deformation problem by applying Central Difference time integration (CDTI) technique for nodal displacements to solve the equation of motion (Zienkiewicz et al., 2005).

The explicit time integration scheme solves the equation of motion by first solving the acceleration $\ddot{u}$ using Newton's Second Law (1.3b). The mass term is replaced by the lumped mass diagonal matrix and the force term consists of external forces F_{ext} and internal forces F_{int}. The acceleration $\ddot{u}$ is then used to solve the velocity $\dot{u}$ and the displacement u along with selected time step Δt. The time step Δt is obtained by calculating the minimum time required for the smallest element deformation that is defined by the characteristic element length L^e and the dilational wave speed C_d (1.3c).

$$[M]\ddot{u} + [D]\dot{u} + [K]u = F \,, \tag{1.3a}$$

$$\ddot{u} = [M]^{-1}(F_{ext} - F_{int}) \,, \tag{1.3b}$$

$$\text{and} \quad \Delta t = \min\left(\frac{L^e}{C_d}\right) \tag{1.3c}$$

The internal forces F_{int} is calculated by integrating the transformed of the strain displacement matrix $[B]$ as shown in (1.4a), which contains the second derivative of the shape function N as shown in (1.4b), multiplied by stresses, $\sigma_{t+\Delta t}$, where can be obtained by multiplying dampening matrix $[D]$ by the strain variable ε as shown in (1.4c), and the strain variable ε is calculated by using (1.4d).

$$F_{int} = \int [B]^T \sigma_{t+\Delta t}\, dV\ , \tag{1.4a}$$

$$[B] = \frac{d^2}{dx^2} N \quad , \tag{1.4b}$$

$$\sigma_{t+\Delta t} = [D]\varepsilon\ , \tag{1.4c}$$

$$\text{and} \quad \varepsilon = \int \frac{\dot{u}_2 - \dot{u}_1}{L^e}\, du \tag{1.4d}$$

Furthermore, one of the external forces F_{ext} can be contact forces which occur when one surface touches another surface. There are two types of contacts problem: the two-body contacts, where two different objects come in contact with each other, and the self-contact problems, in which two surface of the same of different objects come in contact with one to another (Zienkiewicz et al., 2005).Excessive contact, or overclosure, occurs when there is a penetration of a master surface by a slave surface. One way to resolve overclosure is by applying a penalty enforcement method, which is used in FE modeling software. The penalty enforcement method resolves contacts by either decreasing the stiffness at the penetration element or increasing the time step.

Computational Fluid Dynamics

Computational Fluid Dynamics (CFD) simulations provide numerical approximation of equations that govern the fluid motion. CFD consists of three parts: pre-processing, a flow solver, and post processing. During the pre-processing step, the model geometry and meshes are taken as inputs, while flow parameters and boundary conditions are defined. Numerical methods are applied to solve governing equations during the flow solver step. Finally, the desired parameters can be calculated and analyzed from the numerical solutions during the post processing step. The governing equations mainly used in CFD consist of the continuity equation (1.5a) and the three dimensional momentum equations, known as the Navier-Stokes equation (1.5b).The governing equations are solved when the difference in the solution from each of the governing equation meets the convergence criteria.

$$\frac{\partial \rho}{\partial t} + \nabla \cdot \rho \vec{v} = 0 \tag{1.5a}$$

and $$\rho \left(\frac{\partial \vec{v}}{\partial t} + \vec{v} \cdot \nabla \vec{v} \right) = -\nabla p + \nabla \cdot \mathbf{T} + \mathbf{F} \tag{1.5b}$$

Even though CFD is a cost-efficient way, with great control on solving fluid dynamic problems, its accuracy is highly dependent upon model geometry and initial conditions. It is important to specify appropriate boundary conditions and choose the correct type of solver. Accurate material properties such as density and viscosity along with initial condition also need to be correctly addressed.

Experimentation

Investigating hemodynamics inside cerebral aneurysms is commonly accomplished by performing an *in-vitro* study using experimental fluid techniques. *In-vitro* studies are shown to provide detailed measurements of hemodynamic parameters that can be varied and designed according to the need of the study. While experimental work utilizes a greater amount of resources that makes individual case study costly and cumbersome, it can be used as a valuable validation for computational simulation (*in-silico*).

Particle Imaging Velocimetry (PIV)

Particle image velocimetry is a flow visualization technique to determine instantaneous velocity vector fields by measuring the displacements of particles that follow the motion of fluid. The PIV system usually consists of a dual-pulsed laser, CCD cameras, a flow loop seeded with fluorescent particles, and a PIV software package. One way to obtain three dimensional velocity vector fields is by using a stereoscopic PIV. In stereoscopic PIV systems, two viewing directions are captured using two CCD cameras. Each camera captures two frames separated by time *dt*, the first frame for the first laser pulse and the second frame captures the second laser pulse. There are two types of lenses that are mounted within the laser system; spherical and cylindrical lenses. A spherical lens expands the laser into a two dimensional plane and a cylindrical lens expands the laser pulse to form a thin laser sheet. Two dimensional average particle displacements are captured by each frame of the camera. The captured frame is then divided into many smaller interrogation windows of desired size. Each of these interrogation windows are cross correlated to each other and the greatest correlation from two windows will result in a correlation peak that gives the displacement *dx*. The velocity field is finally

calculated by collecting *dt* from the separation time between the laser pulses and *dx* from the cross correlation peak calculation. The PIV process summary is illustrated in Figure 4.

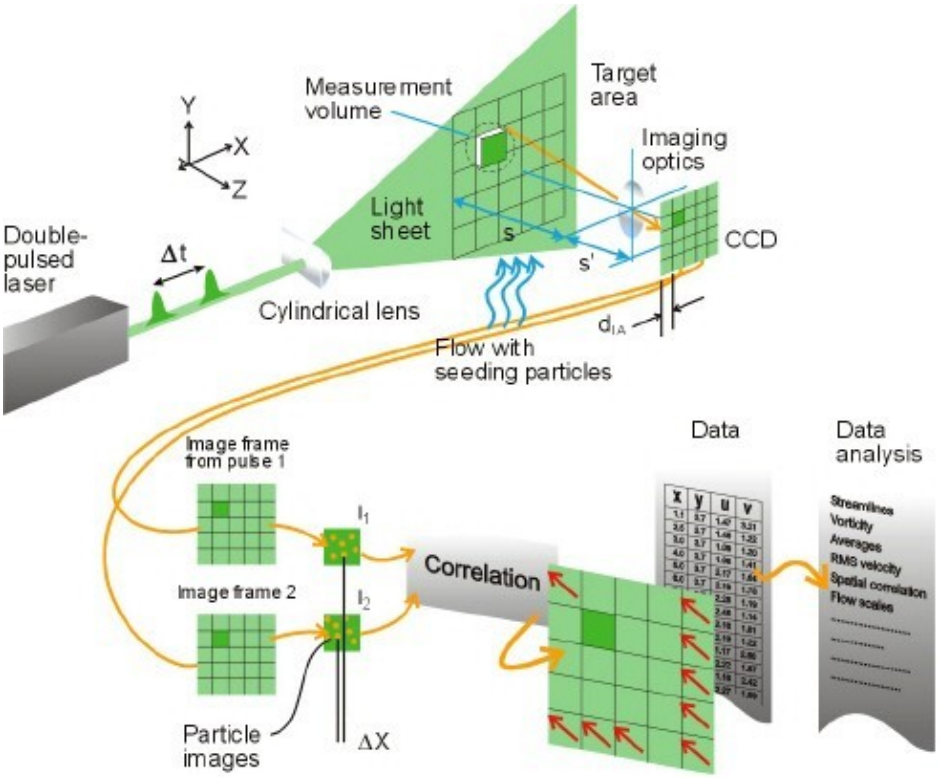

Figure 4. Stereoscopic PIV set up and processes in a nutshell[3].

[3] "Dantec Dynamics - laser optical measurement systems and sensors - Measurement principles." Dantec Dynamics - laser optical measurement systems sensors. http://www.dantecdynamics.com/Default.aspx?ID=1049.

Chapter 2: PREVIOUS WORK

The two treatment options namely surgical clipping and coil embolization have been compared and studied previously in both ruptured and unruptured ICAs. Hwang *et al.* studied the clinical outcome and effects of endovascular coiling and neurosurgical clipping in unruptured ICAs cases (2012). This study was based on a database of research articles published between 1950 and July 2010, and statistical analysis was performed on 24 out of 4160 studies. Surgical clipping was considered to be a more invasive approach to treat unruptured ICAs with up to 2.5 times more neurological and cardiac complications than coiling. The authors concluded that coiling was a better procedure to treat unruptured ICAs due to lesser surgical risks. (Hwang et al., 2012). Furthermore, Lusseveld *et al.* studied the endovascular coiling versus neurosurgical clipping in patients with ruptured BTAs, specifically by comparing aneurysm characteristics, procedural complications, and clinical and anatomical outcomes in 44 coil-treated patients and 44 clip-treated patients (2002). Optimal occlusion achieved by coiling and clipping were successful in 41 patients (93%) and 40 patients (90%), respectively. However, after weighing in the procedural complications occurred in clipping, coil embolization was suggested to be the preferred treatment for ruptured BTAs (Lusseveld et al., 2002).

ICA rupture rates have also been linked with aneurysmal geometry. Two common geometric parameters that have been investigated are aneurysm size and parent vessel (PV) angles. Jeong *et al.* conducted a study of 115 male and 221 female patients with ICAs to determine if there was a critical aneurysm size at which a chance of aneurysm rupture might increase (2009). The results were based on angiograms for 239 ruptured aneurysms and showed that the most prevalent aneurysm size to rupture was 3-6 mm in

the anterior cerebral arteries, the middle cerebral arteries, and the posterior cerebral arteries (Jeong et al., 2009). Furthermore, Ford *et al.* investigated a correlation between BTAs PV angles and their distinct hemodynamic phenotypes using computational fluid dynamics (CFD) (2008). This study looked at PV angles ranging from 2 to 30 degrees in idealized BTAs with a 12 mm and 2.75 mm aneurysm dome and PV diameter, respectively. The PV angle parallel to the inlet of the basilar artery and perpendicular to aneurysmal neck was defined as zero degree. The simulation was under the assumption that the geometry was made out of rigid walls. The results suggested that there were two distinct flow types, or hemodynamic phenotypes. Type I presented with localized wall shear stress (WSS) to the neck of aneurysm while type II presented with more uniform WSS along the anterior wall of the aneurysm, inside the dome. At an angle of 10 degree, the hemodynamic phenotypes changed from type I to type II, and the inflow jet moved closer to the anterior wall as angle increased. Therefore, the authors concluded that PV angle influenced hemodynamic changes in BTAs (Ford et al., 2008).

Coil shape, PD, and aneurysmal geometries are also believed to influence embolic coil treatments success. One way to measure treatment success is by detecting aneurysm recanalization and recurrence. Raymond *et al.* conducted a retrospective analysis of 501 aneurysms cases in 466 patients and found recurrences of 33.6 % of the treated aneurysms post treatments to be most frequent in basilar tip bifurcation (2003). A study by Wakhloo *et al.* reported a low recanalization occurrence at 12.9% from 31 aneurysms patients that were treated by using complex coils alone with packing density of 37% (2007). Different levels of PD were also found to affect hemodynamic changes in an *in-vitro* fluid dynamic study on BTAs done by Babiker *et al.* (2010). A PD level of 28.4% while a PD level of 36.5% were shown to reduce aneurysmal inflow by 31.6% and 49.6% in wide-neck and narrow-neck model, respectively (Babiker et al., 2010). Moreover, Ding

et al. studied the relationship between the aneurysm volume and histologic healing post coil embolization treatments. The correlations between the aneurysm volume, PD, and histologic healing were found significant ($p<0.01$), specifically for smaller aneurysmal volume (Ding et al., 2008).

Wall shear stress (WSS) is often associated with aneurysmal growth and rupture; however, areas of low WSS are associated with thrombus formation. Rayz et al investigated the regions of intra-luminal thrombus deposition in ICAs by quantifying the residence time (RT), which was defined as the time spent by a particle in a domain, and WSS distribution (2010). The study used three patient-specific CFD models of developed BTAs. The results from this study showed that thrombus was likely to form in regions of both low WSS and increased RT (Rayz et al., 2010). Furthermore, in a different study, Rayz *et al.* correlated area of low WSS with regions prone to thrombus formation (2008). The authors hypothesized that thrombus formations were highly affected based on hemodynamic factors. These factors were governed by luminal geometry and blood flow rates. The results from this study suggested that regions of thrombus formation in ICAs corresponded to low flow and low WSS region size (Rayz et al., 2008).

The previous studies had shown that aneurysmal geometric features, such as dome size and PV angle, and embolic coil PD levels had considerable effects on changes in ICA hemodynamic parameter such as WSS and aneurysmal inflow. However, the investigations on the correlation between the aneurysmal geometric features and the hemodynamic changes were studied separately for each different geometrical factor. For instance, the aneurysmal volume alone (Jeong et al., 2009, Ding et al., 2008) or the PV angle alone (Ford et al., 2008) were studied as a single factor instead of a combination of the two. Moreover, the effects of aneurysmal geometric features on coil embolization treatment had not yet been investigated even though coil embolization (Hwang et al.,

2012, Lusseveld et al., 2002) and coil PD level (Babiker et al., 2010) were found to have significant effects on aneurysmal inflow. As previously mentioned, embolic coil sealed aneurysms from blood circulation by promoting thrombus formation within the aneurysmal sac (Geyik et al. 2007). The findings on the area of low WSS in the thrombus regiodue to low flow (Rayz et al., 2008) can be used as an additional parameter to measure the efficiency of coil embolization treatment. Therefore, the purpose of this study is to investigate the influence of a combination of dome size, PV angle, and coil PD on post-treatment aneurysmal hemodynamics by measuring the intraaneurysmal velocity, cross-neck flow and area of low WSS.

Chapter 3: METHODS

Computational Simulation (*in-silico*)

Idealized BTA (IBTA) models were first created using a computer-aided design (CAD) software. These four models were categorized into three different cases: untreated, treated with low coil packing density (LPD) and treated with high packing density (HPD). The untreated models were meshed and assigned boundary conditions, and then were simulated using finite-volume CFD software. An existing finite element (FE) technique to model coil deployments was implemented into this study. Coil deployments in the treated models were simulated using FE modeling software prior to being meshed and computationally solved. Finally, parameters of interest, namely average intraaneurysmal velocity, cross-neck flow, and areas of low WSS were calculated from the CFD solution and analyzed using post-processing software.

Computer-aided Design Model

A total of four IBTA models consisting of a designed combination of dome sizes and PV angles were constructed using SolidWorks (Dassault Systèmes SolidWorks Corp., Waltham, MA, USA) as shown in Figure 5. All models had a 2:1 dome-to-neck diameter ratio. The dome sizes were categorized as small (4 mm) and large (6 mm), and the PV angles were also categorized as small (45 degree) and large (90 degree). The combinations of dome sizes and PV angles for the four models are as follow: 4 mm and 45 degree, 4 mm and 90degree, 6 mm and 45 degree, 6 mm and 90 degree. All aneurysmal domes were modeled as a sphere. A zero degree PV angle was defined parallel to the neck plane. Both the PV inlets and outlets were modeled as cylindrical tube with diameter of 4 mm. The PV inlets in 45 degree models were extruded by 150

mm to satisfy the minimum entrance length requirement to ensure a fully-developed flow (parabolic flow) at the region of interest. The PV outlets in all models were extruded to ensure solution convergence. Entrance length (2.1) is calculated based on the density of the blood analog (ρ), maximum fluid velocity (v), inlet diameter (D) and blood analog viscosity (μ). The density, velocity and viscosity of the blood analog were 1500 kg/m^3, 0.477 m/s and 0.0038 kg/m-s, respectively.

$$L_{entrance} = (0.05\ x\ \frac{\rho v D}{\mu}\ x1000) \tag{2.1}$$

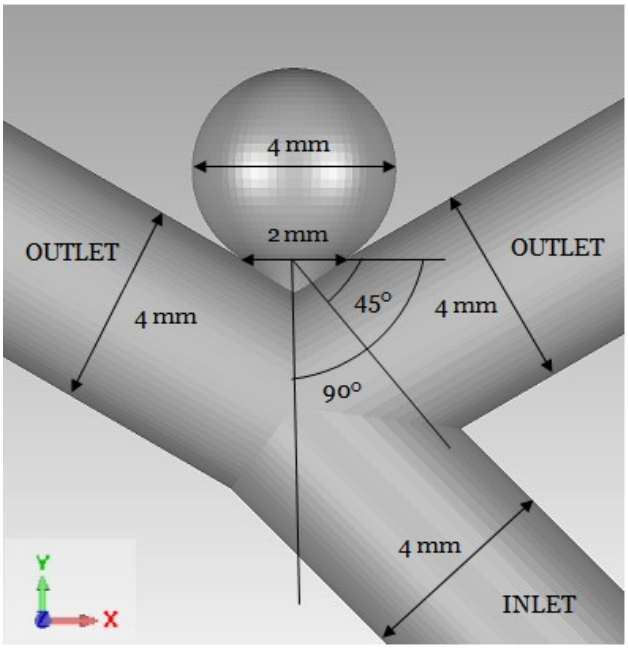

Figure 5. CAD model for IBTA with 4 mm dome size and 45 degree PV angle.

Virtual Coil Deployment

Coil deployments were simulated using Abaqus SIMULIA software (Dassault Systèmes Corp., Waltham, MA, USA). The aneurysmal dome was first isolated from the IBTA model and modified so that the neck plane was curved to imitate the surface of a balloon catheter as shown in Appendix F. The aneurysmal dome model was converted from a surface mesh model to a STP model by using GeoMagic (3D Systems, Rock Hill, SC, USA) and imported into Abaqus. The aneurysmal dome was meshed in Abaqus with

a global seed element size of 1.47 mm. A microcatheter was modeled as a two dimensional wire, and a radial shell surface with a radius of 0.25 mm was created by using a sweeping method. The microcatheter was meshed with a global seed element size of 0.06 mm. Both of the aneurysm and the microcatheter were assigned surfaces and reference points near the aneurysmal neck. The microcatheter was then positioned at the origin with the aneurysmal dome located at the distal point of the microcatheter, away from the origin.

Each coil was created as a three dimensional deformable wire and modeled after the Orbit Galaxy Fill detachable coils (Johnson & Johnson, New Brunswick, NJ, USA). A virtual surface of 0.1524 mm radius surrounding the wire was created and each coil was modeled as a serially linked of 3DTimoshenko beam element (Abaqus element type B31) that includes both rotational and shear deformation. Each coil was assigned a surface, contact nodes and pusher nodes. Reference points were assigned at the midpoint on the long axis of each coil. Material properties for all coils were assigned as follows: Young's modulus of 6.5GPa and 5.5GPa, shear modulus of 0.6 GPa and 0.35 GPa, poison's ratio of 0.319 and 0.319, material densities of 0.02145 g/mm^3 and 0.019 g/mm^3 for coils with a large and small loop diameter, respectively. The coil was meshed with 1.5 x coil diameter element size. The "general contact" algorithm in Abaqus was used to model interactions between coils, the microcatheter, and the aneurysm. The coil-microcatheter interaction was assumed to be frictionless, while the interactions between coil-coil and coil- aneurysm were assumed to have friction coefficients of 0.2 and 0.4, respectively. Lastly, the coil, microcatheter, and aneurysmal dome were positioned in assembly mode, and their interactions were assigned based on the coil deployment step.

Two different coil loop diameter sizes of 4 mm and 2 mm were used. The framing coil, with a larger loop diameter was deployed first, followed by the deployment of a

more pliable coil with a smaller loop diameter to fill up spaces in between the framing coil. Each coil was applied a non-uniform complex coil force distribution as shown in Figure 6 that was modeled as a 3D curve with multiple helical loops rotated around a sphere at different angles (Hung et al., 2005). The force equation to form a complex coils for the small and large loop diameter coils are shown in the Appendix A and B.

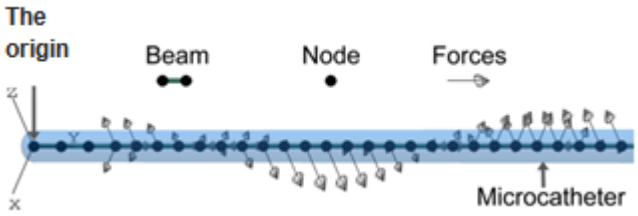

Figure 6. Non-uniform force distribution to prescribe complex coil shape.

Each of the coil deployment process was divided into three steps: coil shaping, coil moving and coil finishing. An initial condition called “encastre” was applied to anchor the aneurysm dome and microcatheter to prevent movements during the deployment process. The initial contact between the coil and the microcatheter was introduced in the coil shaping step. Each coil deployment underwent a total time step of 20 steps and with a period from 0 to 1. A pusher coil boundary condition was assigned to the coil at the node on the origin, and force equations in x, y and z direction were applied along the coil according to the coil loop diameter. The pusher coil boundary condition was modified during the coil moving step to mimic actual coil deployment where the coils were pushed out of the microcatheter. An additional interaction term between the coil and the aneurysm was added to this step so that the coil was contained within the aneurysm dome. Lastly, the coil was released during the coil finishing step and the coil deployment was completed.

Each model underwent two sets of coil deployment processes that represented low and high coil PD. The aneurysms with 4 mm domes had a LPD of 17% and HPD of 26% while the aneurysms with 6 mm domes had a LPD of 18% and HPD of 27%. The combination of coil sizes to achieve the desired PD in each aneurysm model is presented in Table 1.

Table 1. Coil sizes (loop diameter x length) for virtual coil deployment in all four IBTA models.

Model Name/ Coil PD	Low Packing Density (LPD)		High Packing Density (HPD)	
	Coil 1	Coil 2	Coil 3	Coil 4
4 mm, 45^{O}	4 mmx 6.5 cm	2 mm x 2.5 cm	2 mm x 2.5 cm	2 mm x 2.5 cm
4 mm, 90^{O}	4 mm x 6.5 cm	2 mm x2.5 cm	2 mm x 2.5 cm	2 mm x 2.5 cm
6 mm, 45^{O}	4 mm x15 cm	4 mm x 15 cm	2 mm x 10 cm	2 mm x 5 cm
6 mm, 45^{O}	4 mm x15 cm	4 mm x 15 cm	2 mm x 10 cm	2 mm x 5 cm

After the deployment process was complete, each deployed coil was exported as virtual reality modeling language (VRML) file that contains information on the coordinates of the deployed coil's geometry. These coordinates were then paired in a spreadsheet and imported back into Abaqus. After re-sweeping the coil surface with radius of 0.1524 mm and re-meshing the coil with global size of 0.045, the deployed coil geometry was exported again as a VRML file. An additional shrink-wrapping process was done to each deployed coil by using ANSYS ICEM CFD (ANSYS, Inc., Canonsburg, PA, USA). After shrink-wrapping, all holes were repaired by using GeoMagic as shown in Figure 7. Finally, the deployed coil geometry was ready to be meshed along with the complete IBTA model.

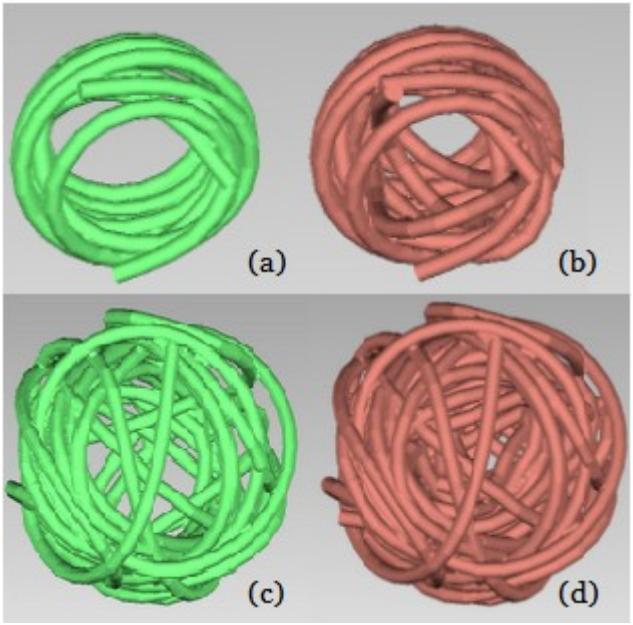

Figure 7. Shrink-wrapped coil CAD model post-deployment for LPD in 4 mm dome size (a) HPD in 4 mm dome size (b) LPD in 6 mm dome size (c) and HPD in 6 mm dome size (d).

Pre-CFD Simulation

All models that are ready to be meshed were imported as a VRML file into ICEM CFD software. The "Build topology" feature was used to concatenate and repair all curves and then the inlet and the outlet surfaces were assigned. Prior the meshing process, the volume of the IBTA model and the coils were created and defined as blood and coil volume, respectively. A box encompassing the region of interest (aneurysm dome and neck) was created and assigned a mesh density function as shown in Figure 8. This defined region allowed finer mesh size elements existed only in the region of interest and coarser mesh in the rest of the model. Therefore, accurate numerical analysis was achieved without sacrificing additional computational time and resources. Each model was assigned global element size, mesh density size, and part mesh size. Combinations of quads/tri elements were used with the Octree meshing method. A mesh convergence

study, which is shown in Appendix C, was performed to determine an ideal mesh size by increasing the size from coarser to finer. Computational simulation was performed at each mesh size, and an ideal mesh size was chosen when a stable solution was obtained, independent from the mesh size. Lastly, boundary conditions were applied and the mesh file was exported from the unstructured mesh file to be solved computationally using finite-volume CFD software.

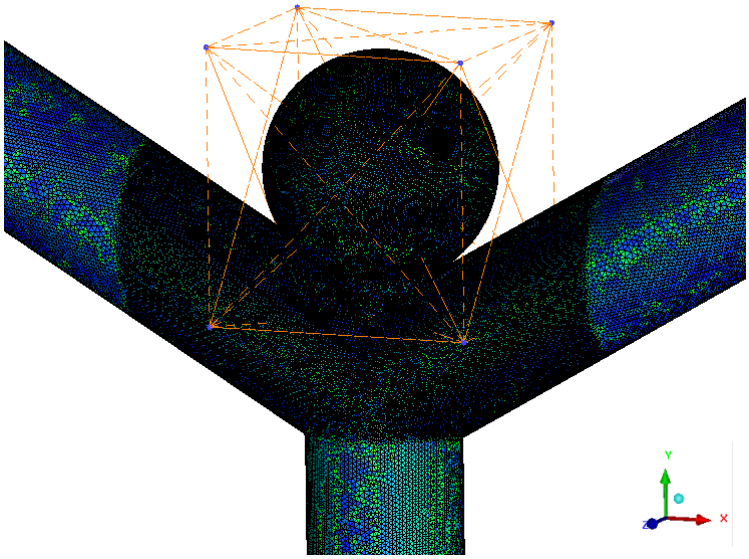

Figure 8. Mesh density function applied within the orange dotted-lined-box surrounding the aneurysmal dome and neck resulting in finer mesh size.

CFD Simulation

All meshed models were imported into ANSYS Fluent v.12 (ANSYS, Inc., Canonsburg, PA, USA) for case set ups and simulated with three different flow rates: 2, 3 and 4 ml/s using Fluent 6.3 (Fluent Inc., Lebanon, NH, USA). All meshed geometries in mesh (MSH) files were opened in ANSYS Fluent v.12, and a grid check was applied to ensure the created mesh topology was adequate. Model scaling was also adjusted to ensure the model geometry magnitudes were correct. Then a case file was written and opened in Fluent 6.3 to simulate. The inlet velocity is defined by calculating the velocity

using PV diameter and flow rate. A user defined function as shown in Appendix D containing the velocity calculation was used for the 90 degree models to ensure fully developed flow at the aneurysmal region. For the 45 degree models, the inlet average velocity was manually entered giving 0.159 m/s, 0.239 m/s and 0.318 m/s for 2, 3 and 4 ml/s flow rates respectively. Operation condition was set to zero Pa. The models were assumed to be rigid with no-slip boundary condition at the vessel walls. The fluid (blood analog) was modeled as a Newtonian, incompressible fluid with density of 1500 kg/m^3 and viscosity of 0.00386 kg/m-s. Gaussian node based solver was used with SIMPLE pressure-velocity coupling to allow more accurate calculation. This solver type was also compatible with the quad/tri element types. Second order upwind momentum and steady implicit method were chosen with convergence criteria of $1e^{-5}$. Finally, the simulation was initialized from the inlet velocity and computed with a maximum number of ten thousands iterations.

Post-CFD Simulation

On achieving convergence, the solution was saved as a case and data file and evaluated using analysis software called Tecplot (Tecplot, Inc., Bellevue, WA, USA). Quantitative hemodynamic parameters were obtained from the aneurysm dome and neck. Average velocity magnitude and area of low WSS were computed from the aneurysm dome and cross-neck flow was examined at the neck plane. For the aneurysmal region, blanking was applied so that everything but the aneurysm dome was excluded from the calculation. The velocity magnitude (2.2a) and WSS magnitude (2.2b) were calculated and then integrated to find their average values. Low WSS values were defined as a 15% of the average WSS magnitude in the untreated cases, and an additional value blanking was applied so that only the region of low WSS remained. Integration

over the area was performed to calculate the area of low WSS. Percent coverage of low WSS area was then calculated by normalizing the low WSS area against its individual surface area of the aneurysmal dome, depending on their sizes.

$$\overline{v} = \sqrt{{v_x}^2 + {v_y}^2 + {v_z}^2} \tag{2.2a}$$

$$\overline{\tau} = \sqrt{{\tau_x}^2 + {\tau_y}^2 + {\tau_z}^2} \tag{2.2b}$$

For the neck plane, a slice from the neck region was extracted and blanked. Cross-neck flow was calculated by taking the absolute value of the velocity that was perpendicular to the neck plane, which accounted the accumulations of all velocity. A mass flow rate function was integrated over the cross neck section assuming the fluid was incompressible (constant density) to calculate the cross neck flow.

Experimentation (*in-vitro*)

Two out of four IBTA models were selected based on a fractional factorial design to be cast into physical urethane models by a lost-core casting technique. The urethane model was mounted on a translational stage in the PIV setup and connected to a flow loop. Flowmeter calibration was performed using a bucket test to ensure output readings were corresponded to correct flow rates. Images for each model were taken prior data acquisition. Camera calibration using a pinhole camera model was performed after each experiment completed. All the recorded images were corrected through an automated camera calibration and self calibration features in a PIV software. Corrected image data was processed to obtain the velocity vector fields. Finally, the processed data file were exported and to be analyzed using MATLAB (MathWorks, Natick, MA, USA).

Physical Model Construction

Two representative IBTA models were selected from the four CAD models that were used in computational simulation. The two selected models geometries were small dome size with small PV angle and large dome size with large PV angles. The selected models were sent to a 3D wax printer, Solidscape (Solidscape, Inc., Merrimack, NH, USA). The wax model was encapsulated in a silica-based investment and subsequently burned out. A low temperature metal was melted and poured into the hollow investment. After the metal core solidified and the outer investment removed, a liquid urethane was cast around the metal core. Finally, the metallic core was melted out resulting a clear hollow IBTA models urethane block as shown in Figure 9.

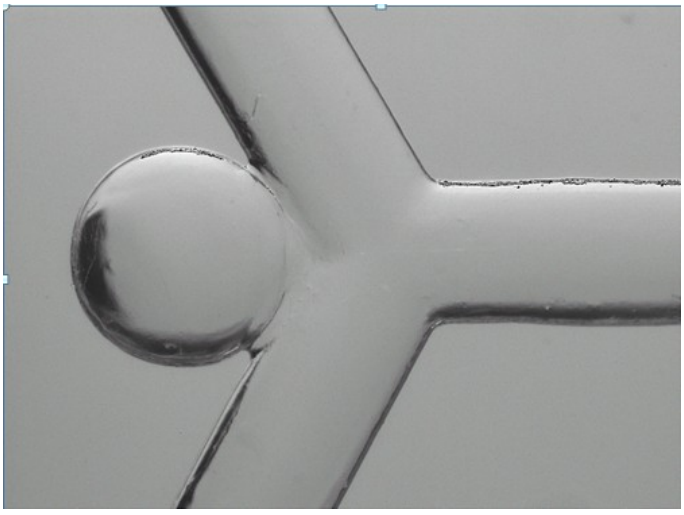

Figure 9. Urethane model for IBTA with 6 mm dome size and 90 degree PV angle.

The Flow Loop

Each of the urethane models was mounted on a micron translation stage and connected to a flow loop using flexible polyvinyl chloride tubing. Acrylic connector tubes of 150 mm in length were attached to the inlet and the outlets to satisfy the required entrance lengths for fully developed flow. The flow loop consisted of a peristaltic pump, a

flow meter, and a reservoir. The peristaltic pump drove fluid in the tubes by using two rollers. As the fluid entered the pump, the rollers pinched part of the tube (void) leaving a trapped fluid in between the rollers (pillow). Alternating pillows and voids caused a discontinuous flow that drove the fluid in a pulsatile manner. A compliance chamber was connected to the flow in order to dampen the pulsatile flow into an almost steady flow. A flow meter (Omega Engineering, Inc., Stamford, CT, USA) was connected downstream to ensure that the desired flow rate through the model was obtained. The voltage output from the flow meter was displayed on a LabView program. A resistance valve was included into the flow loop to control the amount of flow going into the aneurysm model.

An 80% sodium iodide solution with a refractive index of 1.465 is chosen as the blood analog. The blood analog is chosen such that it matches the refractive index of urethane to prevent optical distortion. The density and viscosity of the solution is 1500 kg/m^3 and 0.00386 kg/m-s, respectively. The working fluid is seeded with 8μm Rhodamine-B fluorescent particles (Thermo Scientific, Waltham, MA, USA). These particles absorb the laser light at 532 nm and emit lights at their peak excitation of 542 and 618 nm which were captured by cameras.

The PIV System

Flowmaster 3D stereo PIV system (Lavision, Ypsilanti, MI, USA) with an angular displacement and DaVis software (Lavision, Ypsilanti, MI, USA) were used to capture and display the seeded flow inside the model. Two Imager Intense CCD cameras along with AF Micro-Nikkor 60-mm lenses (Nikon, Tokyo, Japan) with lens f-number of eight were mounted facing the urethane model. Each of the two cameras had a magnification that had been calculated at several different locations in the recorded images based on

the urethane model boundaries. The mean vertical (lateral) and horizontal magnifications were 1.389 and 1.391 respectively for camera one and 1.386 and 1.383 respectively for camera two. A lateral magnification standard deviation for camera one and two are 1.7e-02 and 6.5e-03 respectively. Low-pass filters (Omega Optical, Brattleboro, VT) were installed on the camera lenses with cutoff of 572 nm to capture illuminated particle fluorescence while blocking the excess laser reflections. Solo II Nd:YAG laser (New Wave Research, Fremont, CA, USA), a double-pulsed laser, was mounted on top of the model and used to illuminate flowing particles through the physical model especially in the aneurysm regions. The PIV system set-up is illustrated in Figure 10.

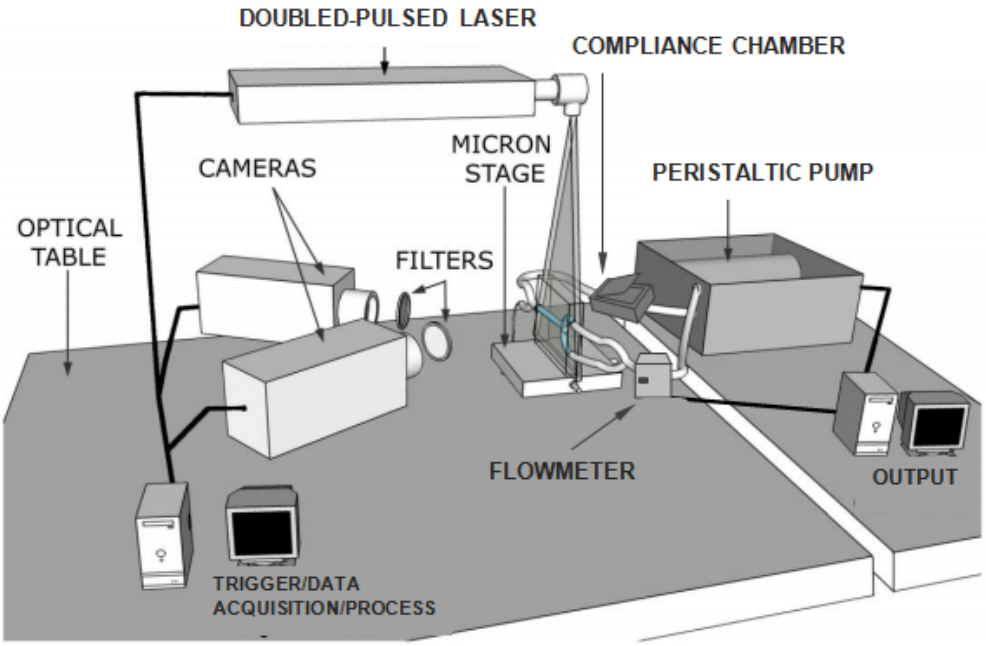

Figure 10. The PIV experimental set-up[4].

[4] Babiker, M.H., L.F. Gonzalez, F. Albuquerque, D. Collins, A. Elvikis, C. Zwart, B. Roszelle, and D.H. Frakes. 2013. "An In Vitro Study of Pulsatile Fluid Dynamics in Intracranial Aneurysm Models Treated with Embolic Coils and Flow Diverters." *IEEE Transactions on Biomedical Engineering* 60 (4): 1150–1159.

Camera calibrations were performed to the stereo PIV system after each data acquisition was complete. A planar glass calibration plate containing precise grid markers was mounted on the micron translation stage where the laser sheet coincided. Images of the calibration plate coinciding with the laser light sheet and a 0.5 mm out-of-plane image were captured for each camera. Multiple markers were manually assigned onto plate images in the first and second camera. A mapping function within DaVis was used to automatically find markers on the plate based on a camera pinhole model. Calibration parameters obtained from completed plate calibration method was used for image corrections. An additional self-calibration technique might be necessary to correct any misalignments and discrepancies.

Device Deployment

TruFill DCS Orbit detachable coils (Codman, Johnson&Johnson Neurovascular) of different sizes were deployed into the urethane model by using microcatheters and a balloon. A total of four coils were deployed into the smaller aneurysm (4 mm, 45 degree angle) model while a total of seven coils were deployed into the larger aneurysm (6mm, 90 degree angle) model. Both models underwent two series of deployment to achieve low and high PD. LPD was calculated to be 19.8% for the smaller aneurysm and 20.4% for the larger aneurysm, while HPD was calculated to be 28.9% for the smaller aneurysm and 30.2% for the larger aneurysm. Coils with larger loop diameter were deployed first then smaller loop diameter coils were deployed last. The coil sizes for each model deployments were explained in Table 2.

Table 2. Coil sizes for physical coil deployment in the urethane IBTA models.

Model name/ Coil PD	Low Packing Density (LPD)			
	Coil 1	Coil 2	Coil 3	
4 mm, 45^{O}	3 mm x 4 cm	3 mm x 3 cm	2 mm x 2 cm	
6 mm, 90^{O}	6 mm x 9 cm	5 mm x 10 cm	4 mm x 12 cm	
	High Packing Density (HPD)			
	Coil 4	Coil 5	Coil 6	Coil 7
4 mm, 45^{O}	2.5 mm x 4.5 cm			
6 mm, 90^{O}	3.5 mm x 5 cm	2 mm x 8 cm	2 mm x 1 cm	2 mm x 1 cm

All coils were deployed under a conventional video camera to provide better viewing. A balloon was deployed through the outflow vessel and placed at the neck. A microcatheter was deployed and placed just above the neck plane. Another microcatheter containing a coil was deployed and placed in the center of the aneurysmal dome. A guide wire that was connected to the coil was pushed forward as the coil was released inside the aneurysm dome. When the coil deployment was nearly finished, a pressure syringe that was filled with de-ionized water was injected into the guide wire to detach the coil from the guide wire completely. This procedure then was repeated for the next sets of coils.

Data Acquisition

Prior to data acquisition, each of the urethane models was mounted on the stage and connected to the flow loop. A total of five planes within the region of interest were acquired at flow rates of 2, 3 and 4 ml/s, and a set of 100 image pairs was captured at a rate of 5 Hz for each plane. The center plane was obtained by adjusting the laser sheet to

coincide with aneurysm dome and neck. Two outer planes and two inner planes with increments of 0.5 were determined to obtain a total of five planes. The CCD cameras placement was adjusted so that the two cameras would capture roughly the same magnification and location of the aneurysmal model. The two laser pulses power percentages were adjusted so that they would have the same intensity in terms of particle brightness. The focal length for each camera was also adjusted to ensure the captured illuminated particles were not blurry. The internal trigger of the laser system was used to capture steady flow data. The variable *dt* was manually determined at each plane of each flow rate by grabbing a sample data and observing particle movements.

Data Processing and Analysis

Upon data acquisition, the corrected images were processed using DaVis post processing options. Mask definition was applied to each image so that the coils and image background were excluded from vector calculations. Vector fields were calculated in each frame by applying a stereo cross-correlation algorithm within the software. Each frame was divided into two steps of interrogation windows. A 32x32 pixels interrogation window was first calculated and a 50% grid overlap was applied to reduce the effective window size into 16 x 16 pixels. A multipass stereo cross-correlation algorithm then was applied to the reduced window. This process was repeated for the rest of 49 image pairs, giving an output of a single average velocity vector field and root mean square error field for each plane. Therefore, there were two velocity fields map consisting of average velocity and root mean square for every acquired set of data per plane for each flow rate upon data processing. These data files were then exported as a Tecplot data files and analyzed using MATLAB.

$$Q_{Neck} = w\, L\, \sum_{i=1}^{n} v_{neck} \tag{2.3}$$

A set of MATLAB scripts, as shown in Appendix E, were used to calculate cross-neck flow (2.3) where w is the window size, L is the laser sheet thickness and $\sum_{i=1}^{n} v_{neck}$ is accumulation of the absolute velocity values across the neck plane with n being the number of data points within one plane. The neck plane was defined by calculating the distance between the fundus (the top of the aneurysmal dome) and the area at the neck where no coils were seen. Then x and y coordinates at the neck were located from the quiver image of the velocity field plot and used to define the neck plane boundaries.

Statistical Analysis

A four factors factorial design analysis on a screening experiment was calculated to determine which factor was significant to the corresponding responses. A list of four factors consisted of dome size, PV angle, coil packing and flow rate was assigned on different categorical levels. Dome size and PV angle had two levels of factor namely small and large, while coil packing and flow rate had three levels of factor namely low, medium and high. The categorical levels for coil packing referred to the untreated, LPD and HPD cases while the categorical levels for flow rate referred to 2, 3 and 4 ml/s. The inputs for the response variables are the intraaneurysmal velocity, cross-neck flow and area of low WSS. Finally, a full factorial and full resolution design analysis was used to calculate the p-value and F-ratio by using JMP software (SAS Institute , Cary , NC, USA). The p-value was used as a measure of how significant each factor on corresponding response variables. A p-value of 0.05 was chosen to be significant; therefore, any factors with p-value less than 0.05 were categorized as statistically significant. An effect test was performed on individual factor by calculating the F-ratio, which represents the ratio of the mean square of the model and the mean square of the error. Large F-ratio means that the model has more effects than the error.

Chapter 4: RESULTS

There are three hemodynamic responses of interest that were calculated from the CFD simulation: intraaneurysmal velocity, cross-neck flow, and area of low WSS. Percent reduction was calculated for the intraaneurysmal velocity and the cross-neck flow by normalizing the treated values against the untreated values. Percent coverage of low WSS area was calculated by normalizing the area of low WSS against the surface area of aneurysmal dome. The results are generally presented in groups of two sets: smaller dome size (4 mm) and larger dome size (6 mm). The lighter shades in following figures correspond to the smaller PV angle (45 degree) model and the darker shades correspond to the larger PV angle (90degree). Blue shades represent the untreated cases while the green shades and red shades represent the LPD and HPD cases, respectively. All CFD results were analyzed statistically by using JMP to quantify the effects of dome size, PV angle, coil packing, and flow rate on intraaneurysmal velocity, cross-neck flow and area of low WSS. Cross-neck flow was also obtained experimentally by using PIV and compared against the CFD results.

Intraaneurysmal Velocity

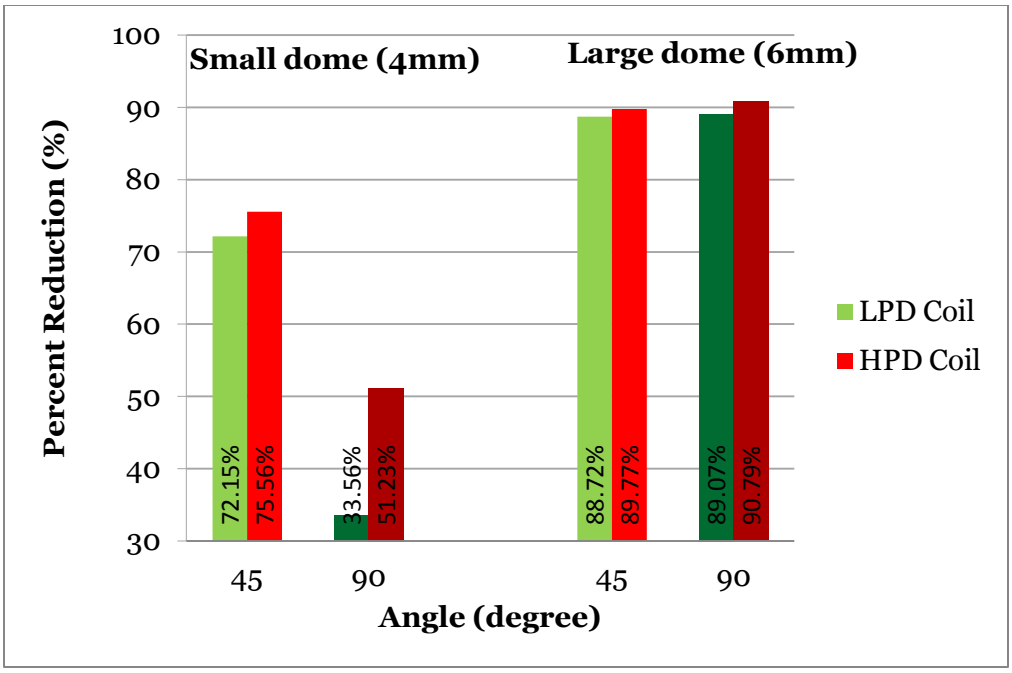

Figure 11. CFD results of the intraaneurysmal velocity percent reduction at 2 ml/s flow rate.

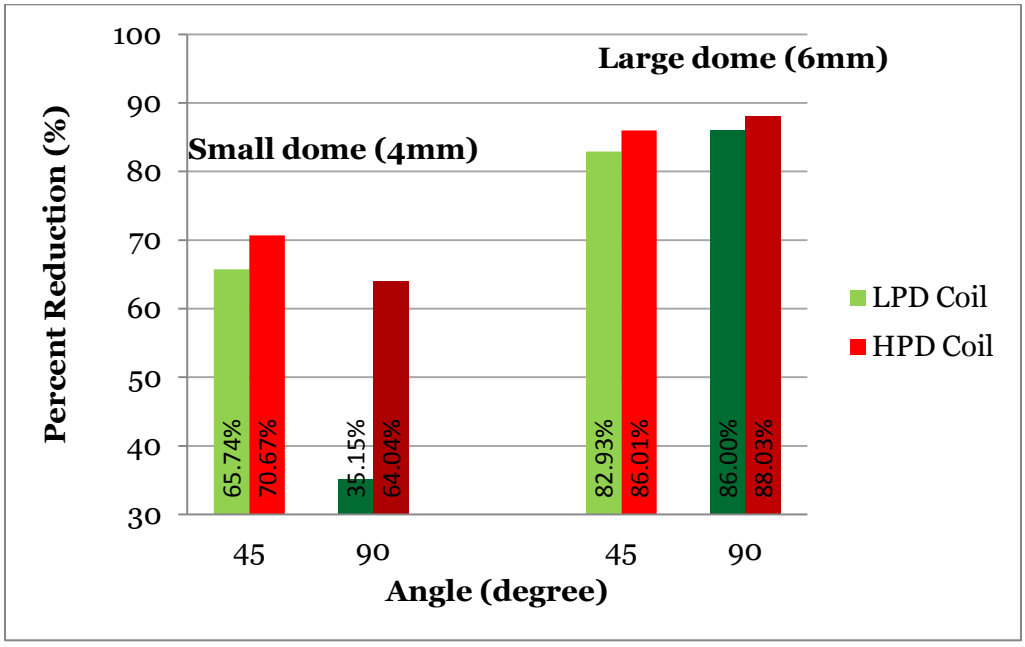

Figure 12. CFD results of the intraaneurysmal velocity percent reduction at 3 ml/s flow rate.

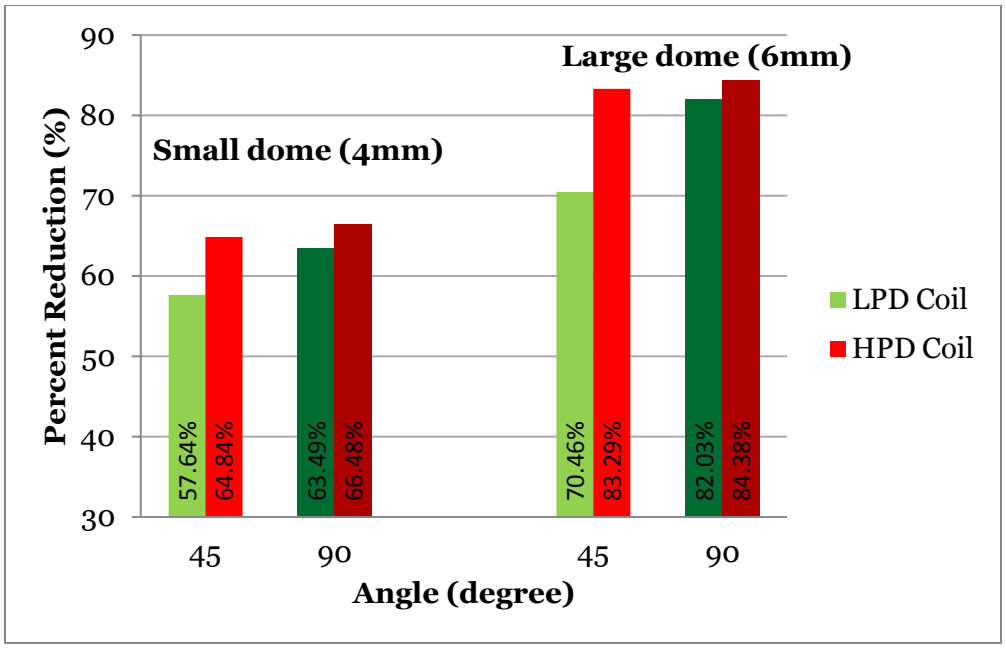

Figure 13. CFD results of the intraaneurysmal velocity percent reduction at 4 ml/s flow rate.

Figure 11, 12, and 13 shows the percent reduction of the intraaneurysmal average velocity in all four IBTA models. Across all three flow rates, aneurysms with the larger dome size have higher percent reduction compared to aneurysms with the smaller dome size. At lower flow rates of 2 and 3 ml/s, a greater relative increase in percent reduction with increase in PD is more apparent in the aneurysms with the smaller dome size compared to the aneurysms with the larger dome size. At 2 ml/s, the largest reduction from low to high PD occurred in aneurysm with small dome size and large PV angle with 18% increase. In the same model, a 30% increase in intraaneurysmal velocity reduction was observed at a higher flow rate of 3 ml/s. However, at the highest flow rate of 4 ml/s, increase in PD seemed to have a greater effect in the aneurysms with small PV angles regardless of the dome sizes. In fact, the largest reduction at 4 ml/s for higher PD was observed in the aneurysm with large dome size and small PV angle.

Cross-neck flow

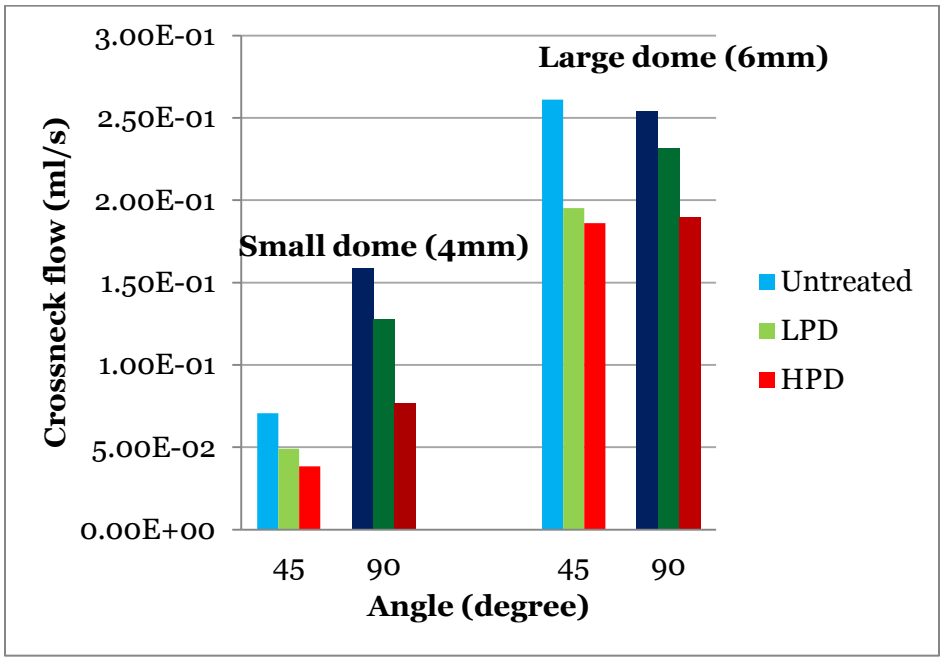

Figure 14. CFD results for the cross-neck flow in the untreated, LPD and HPD cases at 2 ml/s.

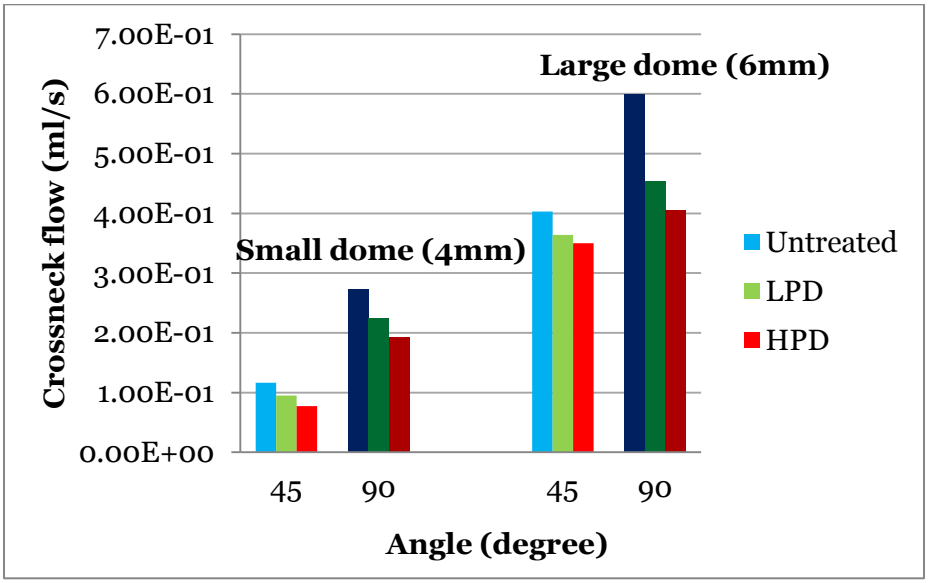

Figure 15. CFD results for the cross-neck flow in the untreated, LPD and HPD cases at 3 ml/s.

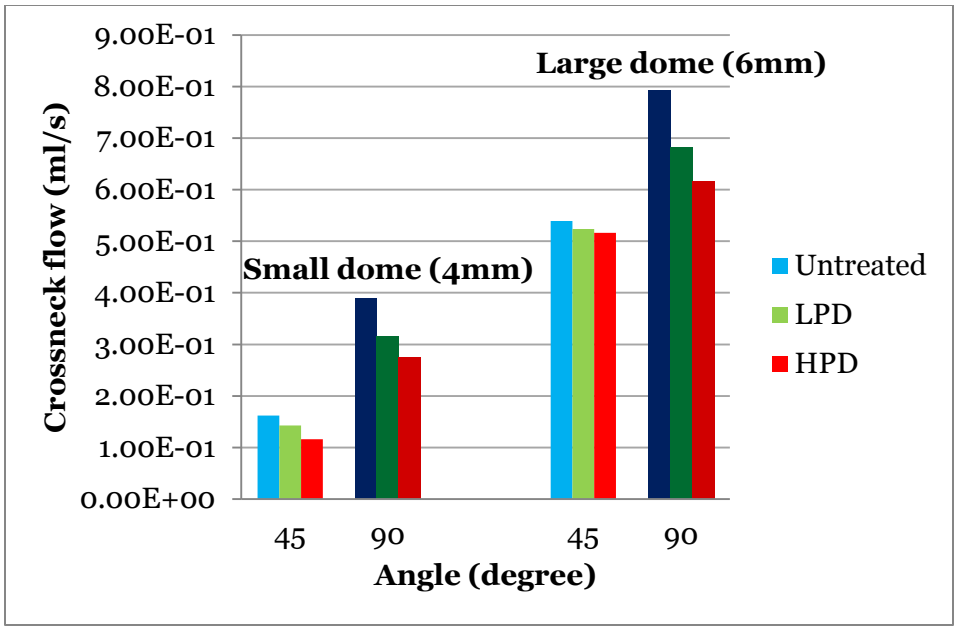

Figure 16. CFD results for the cross-neck flow in the untreated, LPD and HPD cases at 4 ml/s.

Figure 14, 15, and 16 shows the cross-neck flow at 2, 3, and 4 ml/s flow rates. All models show a similar trend at 3 and 4 ml/s, especially for the aneurysms with small PV angles. However, at 2 ml/s, there is a larger drop between the untreated, LPD and HPD cases observed in aneurysms with a small dome and a large PV angle. Since it is difficult to observe the quantified changes associated with each geometric feature, the percent reduction of the cross-neck flow at each flow rate are calculated as shown in figure 17, 18, and 19. Overall, the percent reduction graphs show larger reduction for aneurysms with the smaller dome sizes after coiling. Larger relative effects of higher PD are also observed in aneurysms with the smaller dome sizes.

Furthermore, the cross-neck flow trends show an inconsistent variation among the three flow rates. Aneurysm with the larger dome and smaller PV angle show a decreasing trend in both levels of PD as flow rate increases. At 2 ml/s, the aneurysm with small dome size and large PV angle shows the largest increase in flow reduction (a 32% increase) between the two PD levels. However, at 3 ml/s and4 ml/s, the same model

shows approximately equal increase in flow reduction (a 11% increase) between the two PD levels. This trend is opposite for the aneurysm with small dome size and large PV angle. Increases in percent reduction between the two levels PD are observed in 3 and 4 ml/s compared to in 2 ml/s. However, the aneurysms with small dome size show consistently higher reduction after coiling and as PD level increases. The lowest percent reduction after coiling and the least effect of increasing PD are consistently observed on the aneurysm with large dome size and small PV angle.

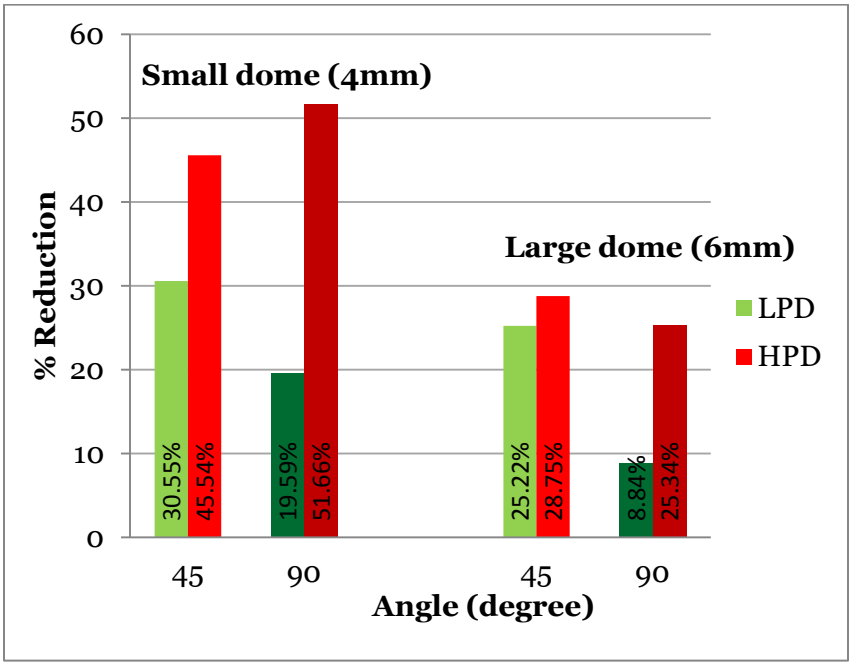

Figure 17. CFD results of the cross-neck flow percent reduction at 2 ml/s.

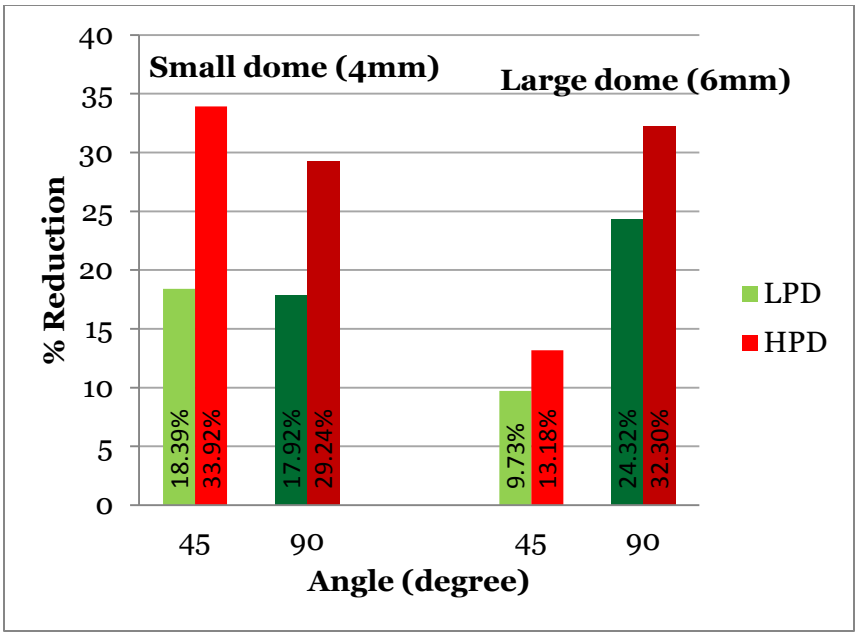

Figure 18. CFD results of the cross-neck flow percent reduction at 3 ml/s.

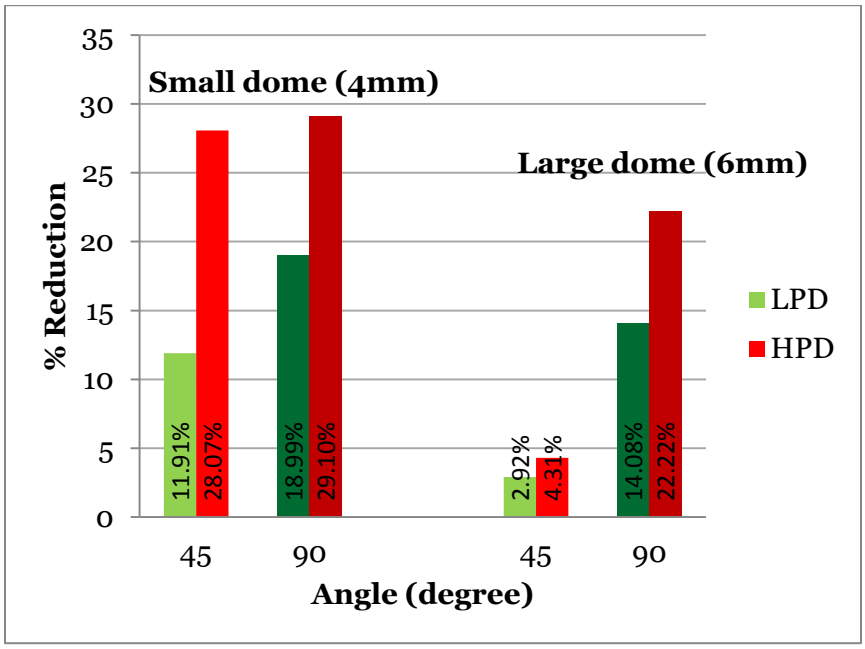

Figure 19. CFD results of the cross-neck flow percent reduction at 4 ml/s.

Wall Shear Stress

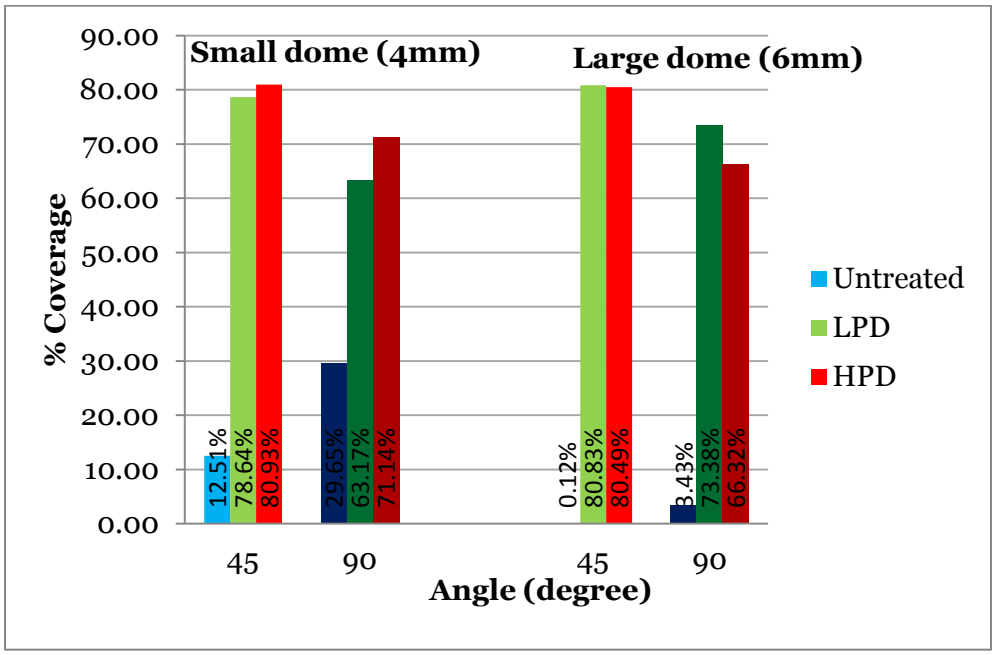

Figure 20. CFD results of low WSS area percent coverage at 2 ml/s.

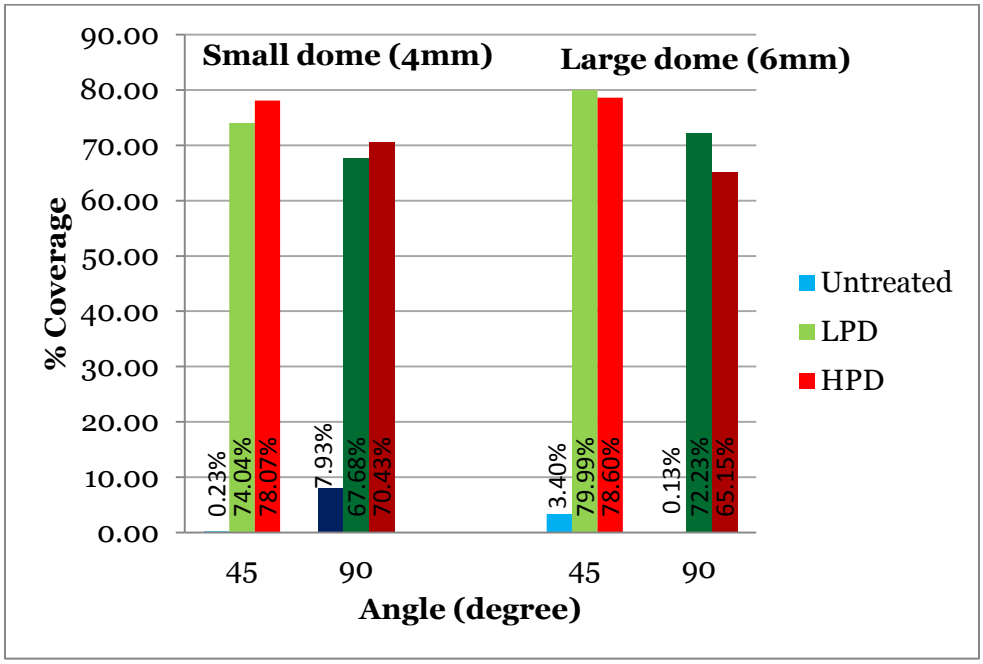

Figure 21. CFD results of low WSS area percent coverage at 3 ml/s.

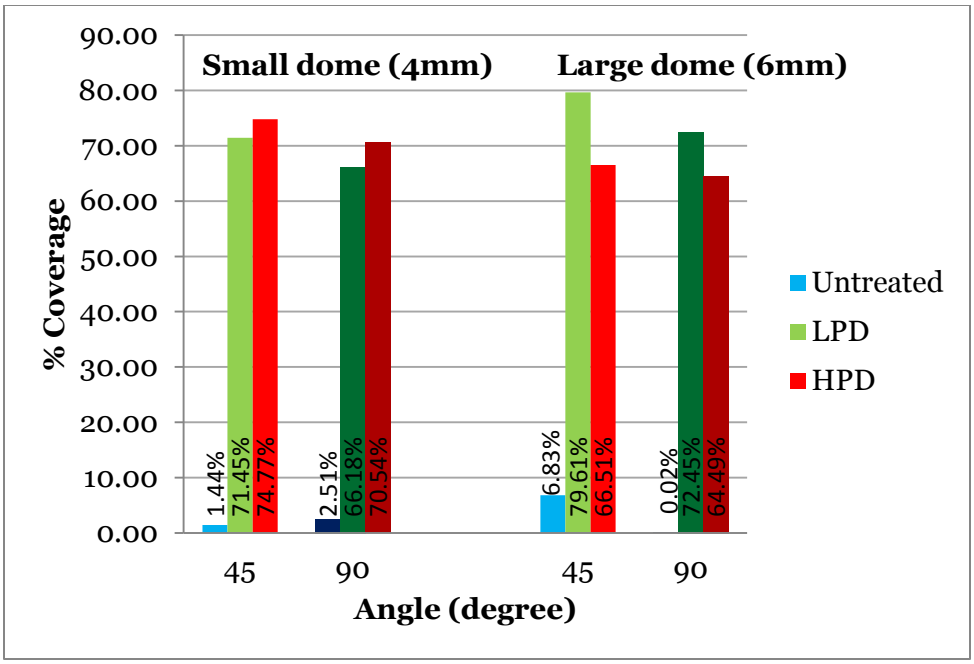

Figure 22. CFD results of low WSS area percent coverage at 4 ml/s.

Figure 20, 21, and 22 show the percent coverage of low WSS area within the aneurysmal dome for 2, 3, and 4 ml/s. Areas of low WSS are greatly increased in the coiling cases compared to the untreated cases in all models. The amounts of percent coverages after coiling were also seen in a similar range between 60-80%. Unlike the intraaneurysmal velocity and the cross-neck flow, the area of low WSS does not change drastically across the three flow rates in all models. However, aneurysms with the smaller PV angle show a slightly larger area of low WSS when comparing to the aneurysms with the larger PV angle. Increasing in area of low WSS as PD increases is only observed in aneurysms with small dome sizes. On the other hand, as PD increases, a decrease in area of low WSS is observed in the aneurysms with larger dome size especially at 4 ml/s flow rate. Overall, coiling treatment showed the greatest relative changes while different levels of PD show little effects on the area of low WSS.

PIV Results

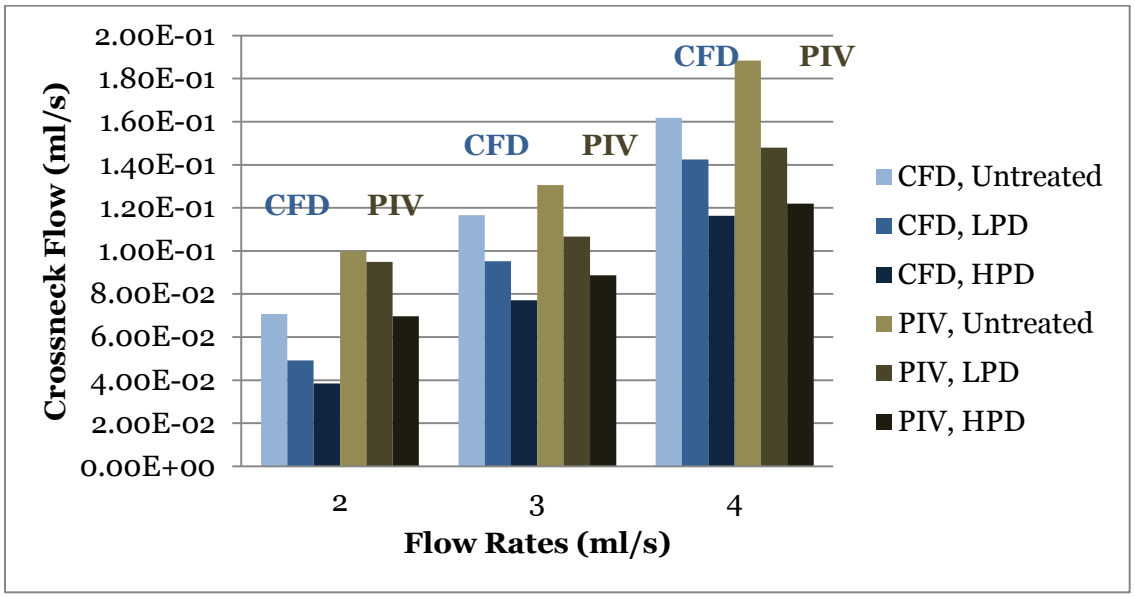

Figure 23. CFD (blue) and PIV (bronze) results for the cross-neck flow in a small dome size (4 mm) and a small PV angle (45 degree)

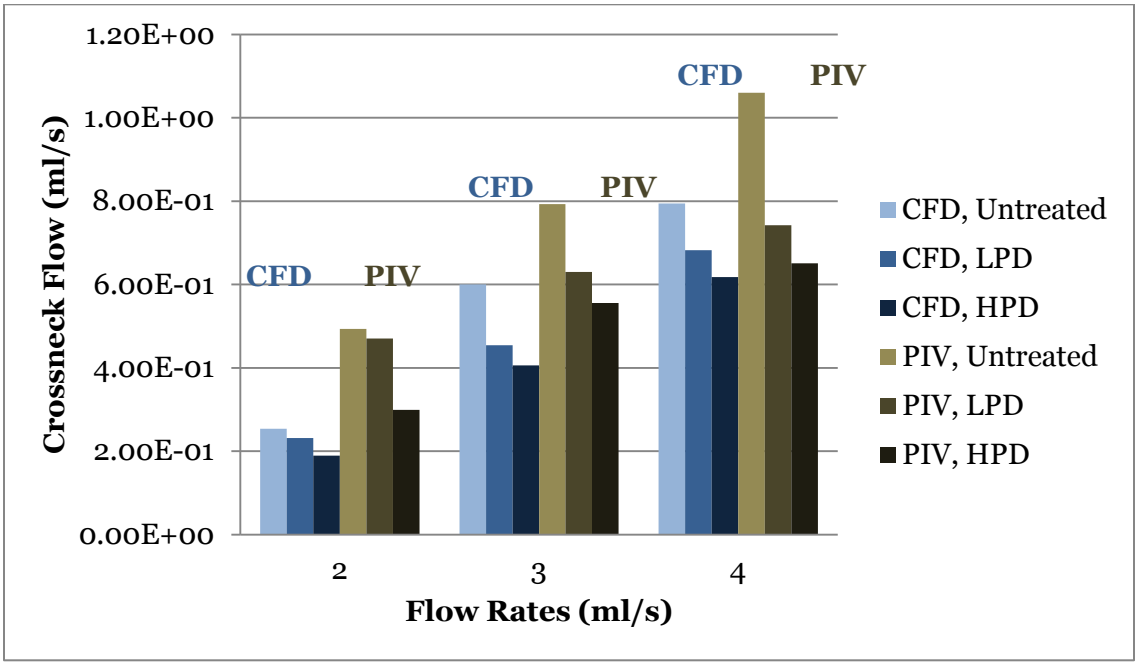

Figure 24. CFD (blue) and PIV (bronze) results for the cross-neck flow in a large dome size (6 mm) and a large PV angle (90 degree) model

Figure 23 and 24 show the CFD cross-neck flow along with the PIV cross-neck flow results for the aneurysm with small dome size and small PV angle, and the aneurysm with large dome size and large angle respectively. Blue shades represent the CFD data and bronze shades represent PIV data. Darker color represents the levels of treatments e.g. the lighter shades correspond to the untreated cases, the semi-darker shades correspond to the LPD cases, and the darkest shades correspond to the HPD cases. The PIV results show that the cross-neck flow in both models increases as flow rate increases, but decreases as coil PD increases in both models. These trends are observed similarly in the CFD results. However, the PIV results are consistently at higher values than the CFD results.

Statistical Results

Table 3. Statistical results for four factors and three responses in all models.

Intraaneurysmal Vel. (F-ratio = 16.77, p-value<0.0001)		
Factor	**F-ratio**	**p-value**
Coil Packing	33.7941*	<.0001
Flow rate	14.1159	<.0001
Dome Size	4.6891	0.0387
PV Angle	0.0822	0.7764
Cross-neck Flow (F-ratio = 41.62, p-value<0.0001)		
Factor	**F-ratio**	**p-value**
Dome size	126.4182*	<.0001
Flow rate	45.1239	<.0001
PV angle	24.7313	<.0001
Coil packing	4.1546	0.0259
Low WSS Area (F-ratio = 149.5, p-value<0.0001)		
Factor	**F-ratio**	**p-value**
Coil packing	443.6602*	<.0001
PV angle	4.5573	0.0414
Flow rate	2.1687	0.1325
Dome size	0.5108	0.4805

Table 3 shows the results for the statistical analysis that was performed in all IBTA models. The model F-ratios are calculated using ANOVA analysis for each response variables giving 16.77, 41.62 and 149.45 for intraaneurysmal velocity, cross-neck flow and area of low WSS, respectively. All three responses have p-value less than 0.0001, indicating that the three responses are significant.

The effect test calculates individual F-ratios and p-values for each factor that corresponds to each response variable. For the intraaneurysmal velocity, coil packing and flow rate show the most significant effect with p-value less than 0.0001. The cross-neck flow, however, is mostly influenced by dome size, flow rate and PV angle with P-value less than 0.0001. Coil packing is shown to be the only significant factor for low WSS area with p-value less than 0.0001.

The F-ratios from each factor are compared to the model F-ratios to determine which factor has the most effect on corresponding response variable. Coil packing has the largest effect on the intraaneurysmal velocity with F-ratio of 33.79. Dome size has the largest effect on the cross-neck flow with F-ratio of 126.42. Lastly, area of low WSS is mostly influenced by coil packing with F-ratio of 443.66.

Chapter 5: DISCUSSION

Average of intraaneurysmal velocity, cross-neck flow and area of low WSS were calculated from CFD simulations, and PIV data were analyzed to validate the simulation results. Results from the CFD simulations for intraaneurysmal velocity and the cross-neck flow showed a similar trend in all IBTA models. There were increasing values as the flow rate increased, and decreasing values as the PD increased. On the other hand, the area of low WSS was greatly affected by the coiling treatment, but minimal changes were observed as flow rate and PD increased. The PIV data validated the CFD data by showing similar trend, even though the PIV values were consistently larger than the CFD data due to discrepancies between the two methods. All results were gathered to draw a conclusion on the relationship between PD and aneurysmal geometric features, namely dome size and PV angle. The statistical results were utilized as a validation tool to all findings by quantifying the largest effect of each factor on each response variables.

Average intraaneurysmal velocity was reduced in all models after coil treatment. This reduction is likely from the coil embolization occupying a portion of the region inside the aneurysmal dome, providing less space for the blood to flow. The velocity reduction was essential for coil treatment because it would eventually lead to flow stagnation and thrombosis. This result confirmed the effectiveness of embolic coils in introducing thrombosis within the aneurysmal sac that eventually helped to occlude the aneurysm from the circulation.

Coil packing and flow rates showed considerable effects in intraaneurysmal velocity reduction after coiling. The velocity was also reduced differently in all models as PD level increased. After coiling, aneurysm with small dome size and large PV angle had the lowest reduction (at 33.56%) compared to the rest of the models. However, this

model had the largest increase with increasing PD. This was probably due to the LPD coil configuration in the smaller dome aneurysm and the inflow jet direction. In smaller dome model with large PV angle, the inflow jet was perpendicular to the neck plane and directed into the center of the aneurysm where no coils presented. Increasing coil PD filled in the non-coiled region at the center of the dome, and, therefore, a large increase was observed in the larger PV angle model for smaller dome aneurysm. Even though the velocity was reduced the greatest after increasing PD, the overall reduction value was still the lowest.

Smaller dome model with large PV angle also showed further velocity reduction with higher flow rate opposing the trend observed in the rest of the models. In other models, the intraaneurysmal velocity reduction decreased as flow rate increased. The decrease in velocity reduction might occur because of an increase in average velocity due to higher flow rate. The increasing in average velocity delayed the stagnant flow because the fluid was moving faster. Therefore, decreases in velocity reduction were observed as flow rate increased due to less clotting formation. This conclusion was supported by the statistical results where the coil packing and flow rate had the greatest effect with F-ratios of 33.79 and 14.11 respectively (p-value <0.0001).

Dome size caused the greatest change in the reduction while no significant difference in velocity was observed with variation of PV angle. This observation might be due to the location of the embolic coil where it occupied inside the aneurysmal dome. Therefore, the variation of dome sizes caused greater changes in the hemodynamic inside the aneurysm after coiling. The statistical results also supported that dome size had a larger significant effect with F-ratio of 4.69 (p-value<0.0387) while PV angle had the least significant effect with the smallest F-ratio of 0.082 (p-value=0.7764).

Even though cross-neck flow showed similar trends to the intraaneurysmal velocity, smaller reductions after coiling were observed in the cross-neck flow than in the velocity across all models. However, the levels of PD have greater effects on cross-neck flow than the intraaneurysmal velocity reduction. For instance, at a lower level of PD, aneurysm with small dome size and small PV angle had 30.55% cross-neck flow reduction while its aneurysmal velocity was reduced by 72.1%. After increasing PD, the cross-neck flow reduction increased from 30.55% to 45.54%, while the intra- aneurysmal velocity reduction increased from 72.1% to 75.56%. While cross-neck flow had a larger increase with increasing PD, the final reduction (45.54%) was still much less than the intraaneurysmal velocity reduction (75.56%). Therefore, coil packing showed the least significant effect among other factors in the cross-neck flow reduction, which was supported by statistical result with F-ratio of 4.15 (p-value<0.0259).

Moreover, the cross-neck flow increase between the different levels of PD was consistently changing across different dome sizes. This might be due to the constant dome to neck size ratio so that the aneurysms with a larger dome size also had a larger neck size. Different neck sizes allowed different amount of flow to pass. Therefore, dome size has a considerable effect in cross-neck flow reduction due to the variation of the neck sizes. This observation was validated against the statistical analysis results where the dome size had the greatest effect on the cross-neck flow variation with F-ratio of 126.42 (p-value <0.0001) comparing to the other factors.

Unlike intraaneurysmal velocity and cross-neck flow, area of low WSS did not show a large variation across different flow rates with increasing PD. The largest considerable difference that was observed on the area of low WSS was between the untreated and the coiling cases. After coiling treatment, the area of low WSS increased by at least 60% in all models. This large difference was supported by the statistical

analysis where coil packing had a significant effect with F-ratio of 443.66 (p-value <0.0001) compared to the rest of the factors. The large increase in area of low WSS might be due to the more uniformly low WSS distribution throughout the wall of the aneurysm dome after coiling. Moreover, the increase in area of low WSS after coiling confirmed an expected correlation between the increasing in aneurysmal velocity reduction and increasing in area of low WSS. Reduced velocity led to flow stagnation and caused less tangential movement against the wall, and, therefore, resulting in lower WSS.

Aneurysms with the larger PV angle showed larger increase in area of low WSS with increasing PD when comparing to the aneurysms with the smaller PV angle. Aneurysms with the larger PV angles also experienced higher reduction as PD increased. On the other hand, the PV flow pattern in the aneurysm with small PV angle was more laminar and, therefore, WSS in the aneurysms with small PV angles after coiling were more uniformly distributed, resulting in huge increase of low WSS area after coiling. However, since the area of low WSS was already largely increased, increasing PD did not show a considerable effect in further increasing the area in aneurysms with small PV angles. The greater effect of PV angle compared to dome size was validated against the statistical results showing F-ratio of 4.55 (p-value<0.0414) and 0.5108 (p-value<0.4805) for PV angle and dome size, respectively.

The cross-neck flow results obtained from the PIV experiment showed a similar trend with the CFD data. Overall, there was an increase in cross-neck flow as flow rate increased, and a decrease in cross-neck flow as PD increased. While the trend of the PIV data was sufficient to validate the CFD results for the cross-neck flow, the PIV results showed consistently larger values across all flow rates and in all models compared to the CFD results. The overestimated values might be due to the discrepancies of the actual

flow condition and in model geometry between the CFD simulation and the PIV experiment. The flow in the experimental model that was captured by the PIV was driven by a peristaltic pump. As previously mentioned, peristaltic pump drove the fluid movement in pulsatile manner. The compliance chamber might not have successfully dampened the pulses completely. Therefore, the undampened flow caused larger inflow and led to greater average velocity at the neck in the PIV data. Larger inflow at the neck in the PIV results was visualized by creating contour plot of the velocity magnitude to compare to the CFD results as shown in Appendix G. Moreover, there was a discrepancy between the CAD model and the urethane model possibly due to shrinkage during model casting stage. As a result, aberrations in the neck size might have caused larger inflow and, therefore, greater average velocity at the neck in the PIV data. Finally, while coil PD for both LPD and HPD in the CAD and the urethane model were not identical, it did not appear to affect large changes in the cross-neck flow. The CAD models had smaller coil PD values by 2% for the LPD cases and 3% for the HPD cases PD values in the urethane models. If the coil PD difference had a large effect, the PIV data would have a variation of cross-neck flow trend when comparing to the CFD data. However, the PIV results were consistently larger than the CFD results confirming a previous conclusion that coil packing had the least effect on cross-neck flow.

Chapter 6: CONCLUSION

This study investigates the effects of aneurysmal geometric features and coil PD on hemodynamics in IBTA models treated with embolic coils. Hemodynamics were simulated using CFD and validated against PIV measurements. An existing FE method to simulate coil deployments was implemented into this study. A total of four IBTA models with a combination of small and large dome size as well as small and large PV angle were treated with two different levels of PD. Three different steady flow rates were applied in all IBTA models. The important conclusions from this work are listed below:

- Intraaneurysmal velocity and cross-neck flow show an increasing trend as flow rate increases
- Coil embolization reduces intraaneurysmal velocity and cross-neck flow while increases area of low WSS
- Increasing coil PD further reduces intraaneurysmal velocity and cross-neck flow
- Area of low WSS increases greatly with initial coiling, but minimal changes result from increasing PD
- PV angle has a statistically significant effect only on cross-neck flow and area of low WSS
- Dome size has the greatest relative effect on cross-neck flow among the factors examined
- Overall, dome size has greater impact on aneurysmal hemodynamics than PV angle
- However, PD has the greatest overall impact on aneurysmal hemodynamics

The findings from this study can be useful as a basis for future study of more realistic models, e.g., anatomical geometry with pulsatile flow, and eventually can be translated into clinical applications such as pre-surgical planning. For instance, patients with larger sizes of aneurysms may not benefit from higher level of PD, and, therefore, can avoid spending additional cost for additional embolic coils. Overall, the results from this study suggested that treatment goals and geometric factors may play key roles in treatment optimization. For example, if the treatment goal is to reduce the velocity inside the aneurysm, higher coil PD may be appropriate to achieve this goal. On the other hand, if the treatment goal is to reduce the cross-neck flow, another endovascular device, e.g, flow diverter may be appropriate to use since cross-neck flow is the least affected with coil packing. Finally, timing may also be a critical factor to decide the effective treatment option. For instance, higher level of coil PD may be more effective in treating aneurysms in early stage since the aneurysmal dome size is small.

REFERENCES

Ashgriz, Nasser, and Javad Mostaghimi. “An Introduction to Computational Fluid Dynamics.” *Fluid Flow Handbook. McGraw-Hill Professional* (2002).

Barrett, Julia. "Cerebral Aneurysm." The Gale Encyclopedia of Medicine 2, no. 3rd ed (2006): 774-778.

Babiker, M. Haithem, L. Fernando Gonzalez, Felipe Albuquerque, Daniel Collins, Arius Elvikis, and David H. Frakes. 2010. “Quantitative Effects of Coil Packing Density on Cerebral Aneurysm Fluid Dynamics: An In Vitro Steady Flow Study.” *Annals of Biomedical Engineering* 38 (7) (July 1): 2293–2301.

Babiker, M.H., L.F. Gonzalez, F. Albuquerque, D. Collins, A. Elvikis, C. Zwart, B. Roszelle, and D.H. Frakes. 2013. “An In Vitro Study of Pulsatile Fluid Dynamics in Intracranial Aneurysm Models Treated with Embolic Coils and Flow Diverters.” *IEEE Transactions on Biomedical Engineering* 60 (4): 1150–1159.

Bederson, J.B., Connolly, E.S., Batjer, H.H., Dacey, R.G., Dion, J.E., Diringer, M.N., Duldner, J.E., Harbaugh, R.E., Patel, A.B., Rosenwasser, R.H., 2009. Guidelines for the management of aneurysmal subarachnoid hemorrhage: A statement for healthcare professionals from a special writing group of the stroke council, american heart association. Stroke 40, 994-1025.

Ding, Yong Hong, Daying Dai, Ramanathan Kadirvel, Debra A. Lewis, Harry J. Cloft, and David F. Kallmes. "Relationship between Aneurysm Volume and Histologic Healing after Coil Embolization in Elastase-Induced Aneurysms: A Retrospective Study." American Journal of Neuroradiology 29, no. 1 (2008): 98-101.

Ford, Matthew D., Sang-Wook Lee, Stephen P. Lownie, David W. Holdsworth, and David A. Steinman. “On the Effect of Parent–aneurysm Angle on Flow Patterns in Basilar Tip Aneurysms: Towards a Surrogate Geometric Marker of Intra-aneurismal Hemodynamics.” Journal of Biomechanics 41, no. 2 (2008): 241–248.

Frosting, M, I Wanke, A Raabe, and V Seifert. "Cerebral aneurysms: Clipping or coiling?." Aktuelle Neurologie 28, no. 3 (2001): 97-102.

Hung, R.K., Loh, C., Goldstein, L., 2005. Selective use of electrolytic detachable and fibered coils to embolize a wide-neck giant splenic artery pseudoaneurysm. Journal of Vascular Surgery 41, 889-892.

Hwang, Jin S., Min K. Hyun, Hyun J. Lee, Ji E. Choi, Jong H. Kim, Na R. Lee, Jin-Won Kwon, and EnJu Lee. “Endovascular Coiling Versus Neurosurgical Clipping in Patients with Unruptured Intracranial Aneurysm: a Systematic Review.” BMC Neurology 12, no. 1 (September 22, 2012): 99.

Jeong, Young-Gyun, Yong-Tae Jung, Moo-Seong Kim, Choong-Ki Eun, and Sang-Hwan Jang. “Size and Location of Ruptured Intracranial Aneurysms.” Journal of

Korean Neurosurgical Society 45, no. 1 (January 2009): 11–15.

Kawanabe, Y., Sadato, A., Taki, W., Hashimoto, N., 2001. Endovascular occlusion of intracranial aneurysms with guglielmi detachable coils: correlation between coil packing density and coil compaction. Acta neurochirurgica 143, 451455.

Krisht, Ali F., Niklaus Krayenb??hl, David Sercl, Kerem Bikmaz, and Paulo A.S. Kadri. 2007. "RESULTS OF MICROSURGICAL CLIPPING OF 50 HIGH COMPLEXITY BASILAR APEX ANEURYSMS." Neurosurgery 60 (2) (February): 242-252.

Lusseveld, E., E. H. Brilstra, P. C. G. Nijssen, W. J. J. van Rooij, M. Sluzewski, C. a. F. Tulleken, D. Wijnalda, R. L. L. A. Schellens, Y. van der Graaf, and G. J. E. Rinkel. "Endovascular Coiling Versus Neurosurgical Clipping in Patients with a Ruptured Basilar Tip Aneurysm." Journal of Neurology, Neurosurgery & Psychiatry 73, no. 5 (November 1, 2002): 591–593.

Przemieniecki, J. S. 2009. Finite Element Structural Analysis : New Concepts. Reston, VA, USA: American Institute of Aeronautics and Astronautics.

Raymond, Jean, François Guilbert, Alain Weill, Stavros A. Georganos, Louis Juravsky, Anick Lambert, Julie Lamoureux, Miguel Chagnon, and Daniel Roy. "Long-Term Angiographic Recurrences After Selective Endovascular Treatment of Aneurysms With Detachable Coils." Stroke 34, no. 6 (June 1, 2003): 1398–1403.

Rayz, V. L., L. Boussel, L. Ge, J. R. Leach, A. J. Martin, M. T. Lawton, C. McCulloch, and D. Saloner. "Flow Residence Time and Regions of Intraluminal Thrombus Deposition in Intracranial Aneurysms." Annals of Biomedical Engineering 38, no. 10 (October 1, 2010): 3058–3069.

Rayz, V. L., L. Boussel, M. T. Lawton, G. Acevedo-Bolton, L. Ge, W. L. Young, R. T. Higashida, and D. Saloner. "Numerical Modeling of the Flow in Intracranial Aneurysms: Prediction of Regions Prone to Thrombus Formation." Annals of Biomedical Engineering 36, no. 11 (November 1, 2008): 1793–1804.

Ross, I. B. and J. D. Fratkin. 2007. "Cerebral Saccular Aneurysm Rupture After Head Injury." The Journal of Trauma 63 (2): E47-50.

Wakhloo, A. K., M. J. Gounis, J. S. Sandhu, N. Akkawi, A. E. Schenck, and I. Linfante. "Complex-Shaped Platinum Coils for Brain Aneurysms: Higher Packing Density, Improved Biomechanical Stability, and Midterm Angiographic Outcome." American Journal of Neuroradiology 28, no. 7 (August 1, 2007): 1395–1400.

Zienkiewicz, O. C.;Taylor, R. L.;Zhu, J.Z., Finite Element Method: Its Basis and Fundamentals, The : Its Basis and Fundamentals (Elsevier Science & Technology, (2005).

APPENDIX A

COIL FORCE DISTRIBUTION EQUATION FOR 2 MM LOOP DIAMETER

Fx_yarn_2_mm

cos(Y*2.8/pow(pi,3))*(sin(Y*2.8/pow(pi,2))*(sin(Y*2.8/pi)*sin(Y*2.8)
+cos(Y*2.8/pi)*0)+cos(Y*2.8/pow(pi,2))*cos(Y*2.8))-
sin(Y*2.8/pow(pi,3))*(cos(Y*2.8/pi)*sin(Y*2.8)-sin(Y*2.8/pi)*0)

Fy_yarn_2_mm

sin(Y*2.8/pow(pi,3))*(sin(Y*2.8/pow(pi,2))*(sin(Y*2.8/pi)*sin(Y*2.8)
+cos(Y*2.8/pi)*0)+cos(Y*2.8/pow(pi,2))*cos(Y*2.8))+cos(Y*2.8/pow(pi,3))*(cos(Y*2.8/pi)
*sin(Y*2.8)-sin(Y*2.8/pi)*0)

Fz_yarn_2_mm

cos(Y*2.8/pow(pi,2))*(sin(Y*2.8/pi)*sin(Y*2.8)+cos(Y*2.8/pi)*0)-
sin(Y*2.8/pow(pi,2))*cos(Y*2.8)*cos(Z)

APPENDIX B

COIL FORCE DISTRIBUTION EQUATION FOR 4 MM LOOP DIAMETER

Fx_yarn_4 (framing)

sin(Y*1.4/pow(pi,3))*(sin(Y*1.4/pow(pi,2))*(sin(Y*1.4/pi)*sin(Y*1.4)
+cos(Y*1.4/pi)*0)+cos(Y*1.4/pow(pi,2))*cos(Y*1.4))+cos(Y*1.4/pow(pi,3))*(cos(Y*1.4/pi)*s
in(Y*1.4)-sin(Y*1.4/pi)*0)

Fy_yarn_4

sin(Y*1.4/pow(pi,3))*(sin(Y*1.4/pow(pi,2))*(sin(Y*1.4/pi)*sin(Y*1.4)
+cos(Y*1.4/pi)*0)+cos(Y*1.4/pow(pi,2))*cos(Y*1.4))+cos(Y*1.4/pow(pi,3))*(cos(Y*1.4/pi)*s
in(Y*1.4)-sin(Y*1.4/pi)*0)

Fz_yarn_4

cos(Y*1.4/pow(pi,2))*(sin(Y*1.4/pi)*sin(Y*1.4)+cos(Y*1.4/pi)*0)-
sin(Y*1.4/pow(pi,2))*cos(Y*1.4)*cos(Z)

APPENDIX C

MESH CONVERGENCE STUDY

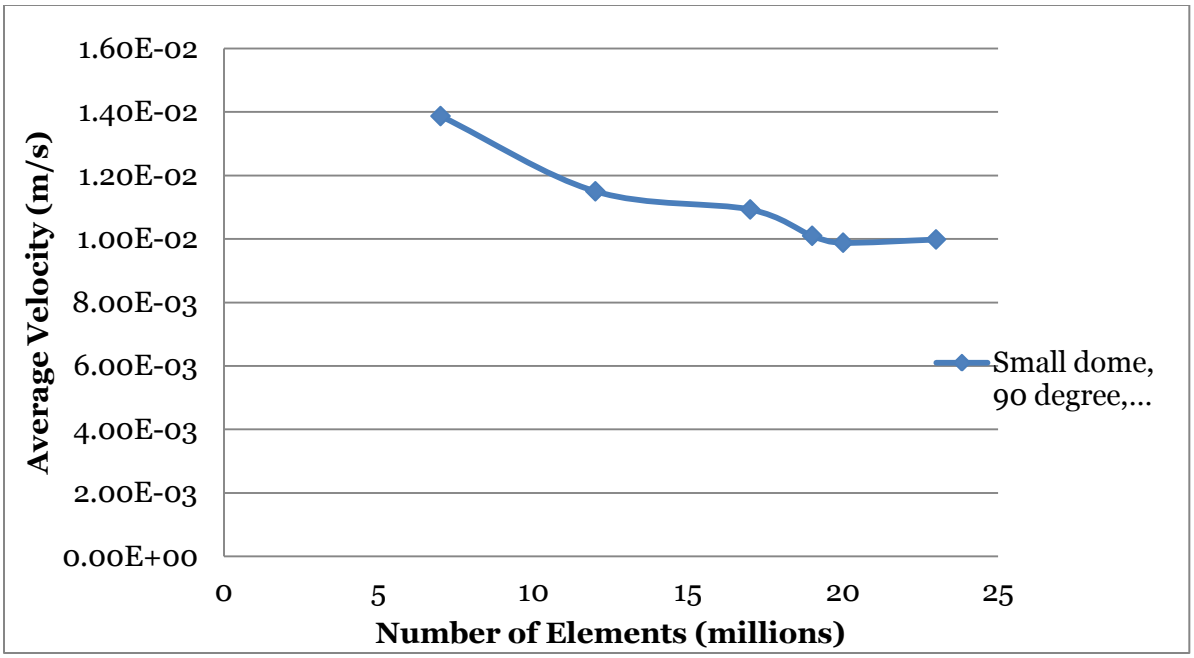
1.60E-02
1.40E-02
1.20E-02
1.00E-02
8.00E-03
6.00E-03
4.00E-03
2.00E-03
0.00E+00
Average Velocity (m/s)
0
5
10
15
20
25
Number of Elements (millions)
Small dome, 90 degree,...

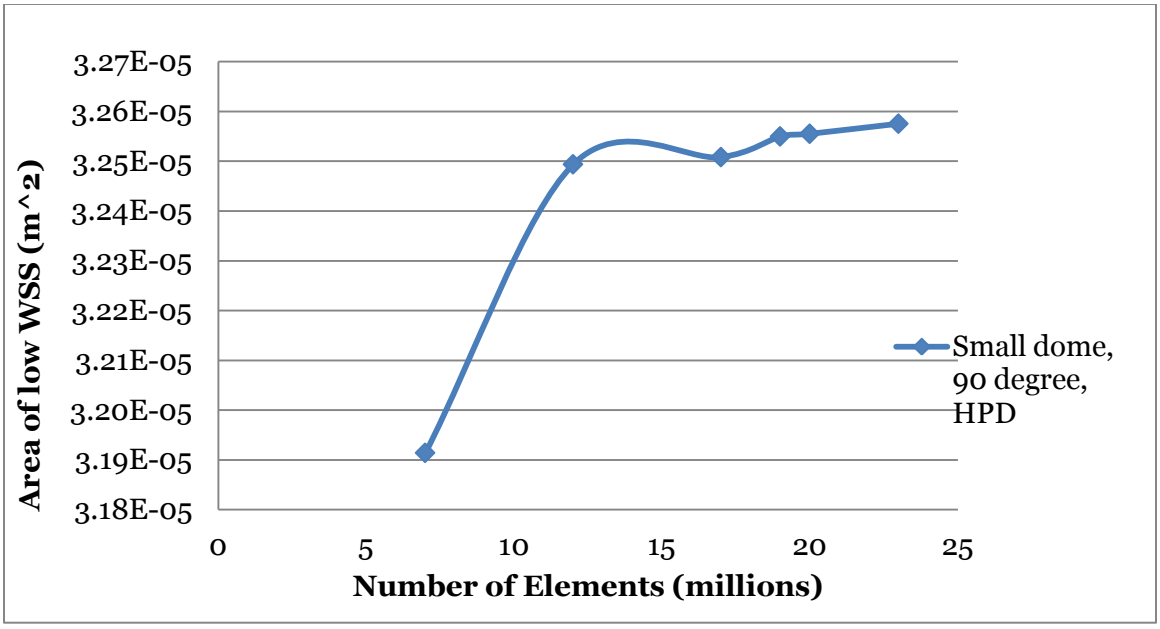
3.27E-05
3.26E-05
3.25E-05
3.24E-05
3.23E-05
3.22E-05
3.21E-05
3.20E-05
3.19E-05
3.18E-05
Area of low WSS (m^2)
0
5
10
15
20
25
Number of Elements (millions)
Small dome, 90 degree, HPD

APPENDIX D

USER DEFINED FUNCTION FOR INLET VELOCITY

```
#include "udf.h"
#define PIPE_DIAMETER 4e-3 // Parent vessel diameter in meters
#define AVG_Y_VELOCITY 0.239// Average y velocity at inlet in m/s for 2 mlps
DEFINE_PROFILE(paraboloid_velocity, thread, position) { real x[ND_ND];
real coeff,r,v_max;
face_t f;
r = PIPE_DIAMETER/2.; //Calculating radius
v_max = 2.*AVG_Y_VELOCITY; //Calculating paraboloid vertex z (max velocity)
coeff = -v_max/pow(r,2.);
begin_f_loop(f, thread)
{
F_CENTROID(x,f,thread);
F_PROFILE(f, thread, position) = coeff*(pow(x[0],2.) + pow(x[2],2)) + v_max;
} end_f_loop(f, thread) }
#include "udf.h"
#define PIPE_DIAMETER 4e-3 // Parent vessel diameter in meters
#define AVG_Y_VELOCITY 0.318// Average y velocity at inlet in m/s for 3 mlps
DEFINE_PROFILE(paraboloid_velocity, thread, position) { real x[ND_ND];
real coeff,r,v_max;
face_t f;
r = PIPE_DIAMETER/2.; //Calculating radius
```

```
v_max = 2.*AVG_Y_VELOCITY; //Calculating paraboloid vertex z (max velocity)
coeff = -v_max/pow(r,2.);
begin_f_loop(f, thread)
{
F_CENTROID(x,f,thread);
F_PROFILE(f, thread, position) = coeff*(pow(x[0],2.) + pow(x[2],2)) + v_max;
} end_f_loop(f, thread) }
#include "udf.h"
#define PIPE_DIAMETER 4e-3 // Parent vessel diameter in meters
#define AVG_Y_VELOCITY 0.318// Average y velocity at inlet in m/s for 4 mlps
DEFINE_PROFILE(paraboloid_velocity, thread, position) { real x[ND_ND];
real coeff,r,v_max;
face_t f;
r = PIPE_DIAMETER/2.; //Calculating radius
v_max = 2.*AVG_Y_VELOCITY; //Calculating paraboloid vertex z (max velocity)
coeff = -v_max/pow(r,2.);
begin_f_loop(f, thread)
{
F_CENTROID(x,f,thread);
F_PROFILE(f, thread, position) = coeff*(pow(x[0],2.) + pow(x[2],2)) + v_max;
} end_f_loop(f, thread) }
```

APPENDIX E

MATLAB MAIN SCRIPTS TO CALCULATE PIV RESULTS

```
clear all
clc
% clf

%Set parameters

%Insert x and y limits
xmin=[-3.33,-3.33,-3.44,-3.56,-3.67];          %min x limit of the aneurysm
ymin=0.4695;                        %min y limit of the aneurysm
xmax=[-3.216,-3.216,-3.326,-3.446,-3.556];         %max x limit of the aneurysm
ymax=2.4695;                         %max y limit of the aneurysm

LS=0.5;                              %laser sheet width in mm
WS=0.113;                           %size of window in mm
FR=[2 3 4];                                                 %Flow rates/named flow rate folders
planes={'plane1','plane2','plane3','plane4','plane5'}; %will set number and name of the planes
time=[280];
dt=300;
%set either PC=1 or MAC=0
Syst=1;
%set anatom 1 to do anatomical models with strange neck planes
anatom=0;
%set the main directory where the dat files
   if (Syst==0)
      cd('/Users/mbabiker/Desktop/FD Stents 2/0 stent/Upstream/constant') %MAC
   else
      %cd('S:\ipalab share\Aneurysm\PIV_results\A_BTA_1\Untreated\steady') %PC
      cd ('S:\ipalab share\AHA_IBTA\DaVis_Export\IBTA_3_Coil_High\Pulsatile')
   end

%remove old files
   checkd=exist('AnVrms_Results');
   checkdv=exist('AnVrms_Results');
   if (checkd==7)
      rmdir('AnVrms_Results','s');
      rmdir('AnVrms_Vort','s');
      rmdir('AnVrms_Intrfl','s');

   end


%add functions from AnVrms into path
```

```
   if (Syst==0)
      path(path,'/Users/mbabiker/AnVrms') %MAC
   else
      path(path,'C:\Users\ryndh\Documents\MATLAB\Anvrms\Anvrms') %PC
   end

%create a new folder to save results
   mkdir('AnVrms_Results')
   mkdir('AnVrms_Vort')
   mkdir('AnVrms_Intrfl');

   head1={'x';'y';'z';'Vx';'Vy';'Vz'};
   head2={'Flow rate';'Vrms'};


for i=1:length(FR)

   for j=1:length(planes)

      %set the plane folder
         if (Syst==0)
%              foldp=strcat( int2str(FR(i)), '/',planes(j)); %MAC
             foldp=strcat( int2str(FR(i))); %MAC
         else
            %foldp=strcat( int2str(FR(i)), '\',planes(j)); %PC
            foldp=strcat( int2str(FR(i)), '\',planes(j),'\',int2str(time(1))); %PC

         %Velocity
         if (Syst==0)
            filnam1=strcat('AnVrms_Results/',int2str(FR(i)),'_',planes(j),'.dat'); %MAC
         else
            filnam1=strcat('AnVrms_Results\',int2str(FR(i)),'_',planes(j),'.dat'); %PC
         end
         filnam1=strvcat(filnam1);
         fid=fopen(filnam1,'wt');
         for k=1:length(xa);
            fprintf(fid,'%12.8f \t %12.8f %12.8f \t %12.8f %12.8f \t %12.8f \t
%12.8f\n',xa(k),ya(k),za(k),Vxa(k),Vya(k),Vza(k),Vmag2(k));
         end
         fclose('all');
```

```
        %Velocity
        if (Syst==0)
           fid2=fopen('AnVrms_Results/Vrms_planes.dat','at+'); %MAC
        else
           fid2=fopen('AnVrms_Results\Vrms_planes.dat','at+'); %PC
        end
        fprintf(fid2,'%3.1f \t %s \t %12.8f\n', FR(i),strvcat(planes(j)), Vrmsa);
        fclose('all');
        VmagT(j)=Vmag;
        lengV(j)=lenVmag;
        Anflow(j)=Infl;
       lengA(j)=lenVmag_actual;
       VmT(j)=Vm;

        %Intra-aneurismal flow
        if (Syst==0)
           fid2=fopen('AnVrms_Intrfl/Intrfl_planes.dat','at+'); %MAC
        else
           fid2=fopen('AnVrms_Intrfl\Intrfl_planes.dat','at+'); %PC
        end
        fprintf(fid2,'%3.1f \t %s \t %12.8f\n', FR(i),strvcat(planes(j)), Infl);
        fclose('all');

    end
        %Velocity
        if (Syst==0)
           fid3=fopen('AnVrms_Results/Vrms_Total.dat','at+'); %MAC
        else
           fid3=fopen('AnVrms_Results\Vrms_Total.dat','at+'); %PC
        end
        fprintf(fid3,'%3.1f \t %12.8f \t %12.8f \t %12.8f \n', FR(i),
sqrt(sum(VmagT)/(sum(lengV))),sum(VmagT), sum(VmT)/sum(lengA));
        %fprintf(fid3,'%3.1f \t %12.8f %12.8f \n', FR(i), sum(Vmag2n),mean(Vmag2n));
        fclose('all');          %Anflow
        if (Syst==0)
           fid3=fopen('AnVrms_Intrfl/Intrflow_Total.dat','at+'); %MA
        else
           fid3=fopen('AnVrms_Intrfl\Intrflow_Total.dat','at+'); %PC
        end
        fprintf(fid3,'%3.1f \t %12.8f \n', FR(i), sum(Anflow));
        fclose('all');
```

```
end
   sum(length_V(i))

%Graph the set at different flow rates
grapa(Syst,length(planes),length(FR))
```

APPENDIX F

ANEURYSM CAD MODEL WITH BALOON SURFACE AT THE NECK

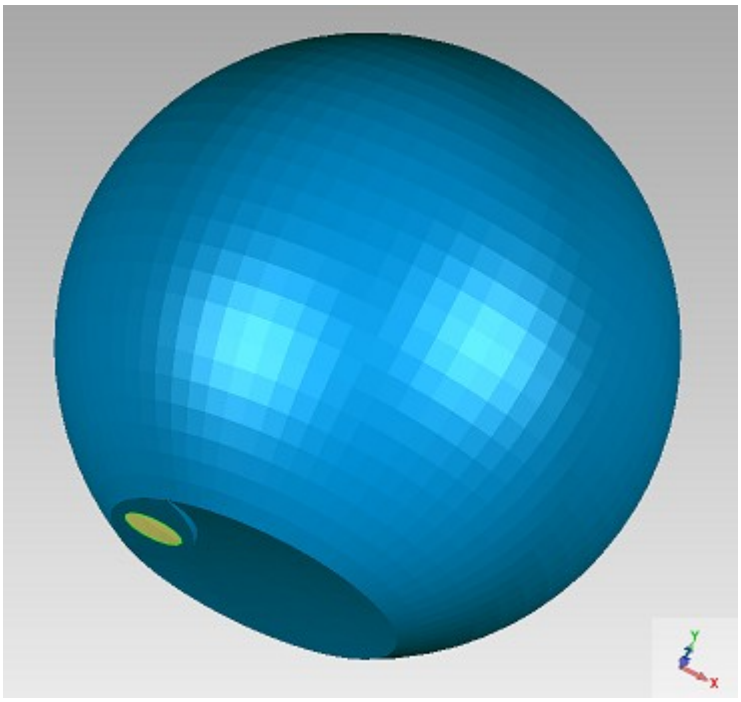
Y
Z
X

APPENDIX G

VELOCITY MAGNITUDE CONTOUR PLOTS: CFD VS. PIV

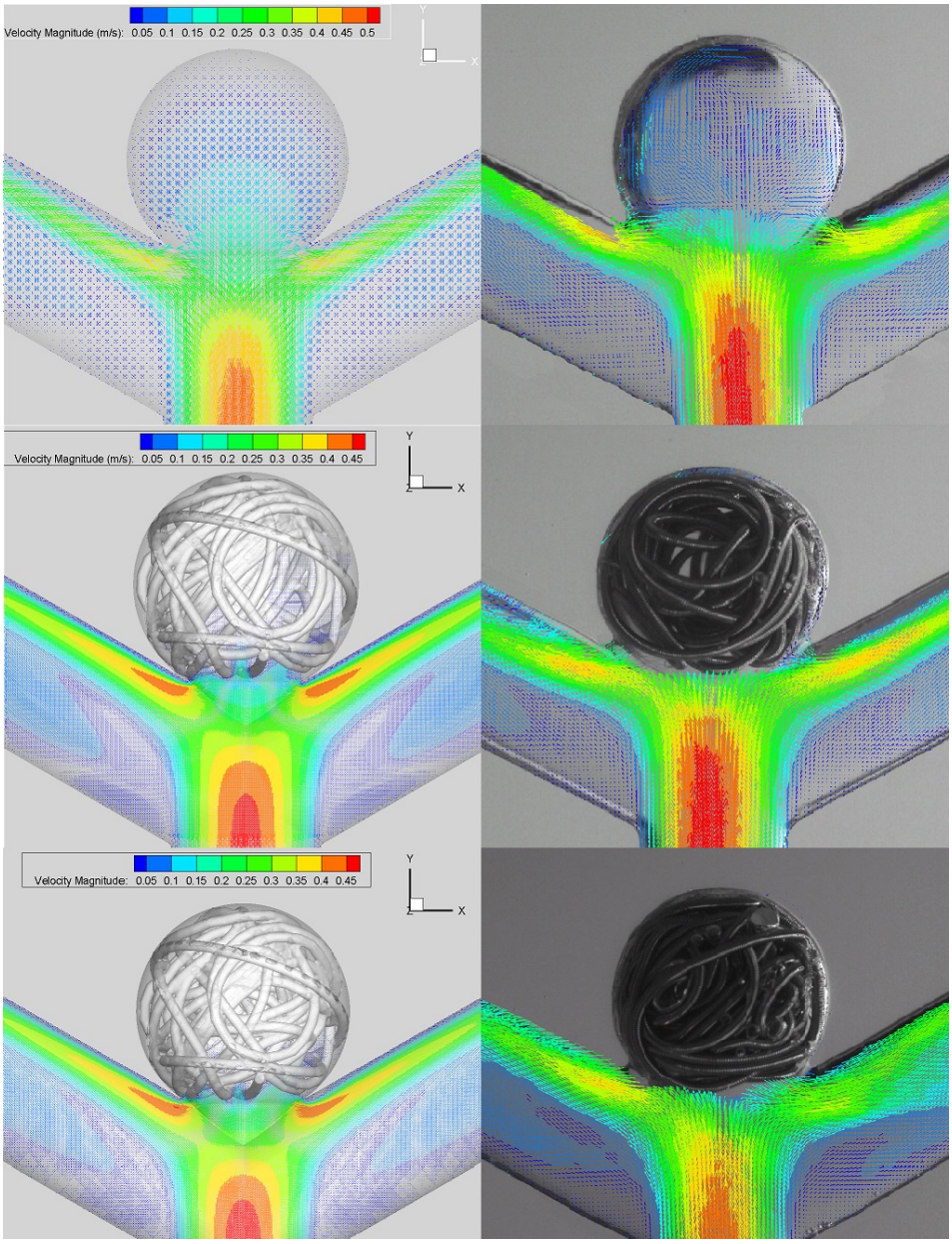
Velocity Magnitude (m/s): 0.05 0.1 0.15 0.2 0.25 0.3 0.35 0.4 0.45 0.5
Y
X
Velocity Magnitude (m/s): 0.05 0.1 0.15 0.2 0.25 0.3 0.35 0.4 0.45
Y
Z
X
Velocity Magnitude: 0.05 0.1 0.15 0.2 0.25 0.3 0.35 0.4 0.45
Y
Z
X